JMEPEG
https://doi.org/10.1007/s11665-024-09388-5

1059-9495/$19.00

ORIGINAL RESEARCH ARTICLE

Surface CuAl9Mn2/W Composites Prepared by Multipass Friction Stir Processing: Microstructures, Phases, and Mechanical and Tribological Properties

Andrey Cheremnov, Anna Zykova, Nickolai Savchenko, Evgeny Knyazhev, Natalya Semenchuk, Denis Gurianov, Andrey Vorontsov, Veronika Utyaganova, Andrey Chumaevskii, Evgeny Kolubaev, and Sergei Tarasov

Submitted: 27 October 2023 / Revised: 4 February 2024 / Accepted: 13 February 2024

This article discusses the structural evolution, mechanical characteristics and tribological behaviors of CuAl9Mn2 + W surface composites containing 0, 5, 10 and 15 vol.% W prepared using both 1-pass and 4-pass friction stir processing. Homogeneous distribution of W-particles in the bronze matrix has been achieved using the 4-pass FSP. According to XRD, the following phases have been formed in the FSPed bronze matrix: α-Cu solid solution, α + β'-Cu_3Al eutectoid, and γ-Al_4Cu_9 laths. Adding tungsten in FSP resulted in enriching the samples with γ-Al_4Cu_9. Formation of γ-Al_4Cu_9 occurred according to the well-known equilibrium reaction $\beta \rightarrow \alpha + \gamma$ and may be related to some physical characteristic of the composite that changed with the addition of tungsten. In our opinion, this could be the reduced heat conductivity that made some β-Cu_3Al grains to decompose into α-Cu and γ-Al_4Cu_9 ones instead of the $\beta \rightarrow \beta'$ transformation. The mean sizes of the α-solid solution matrix grains after 1-pass and 4-pass FSP were at the level of 4.48-7.54 μm and 3.47-5.43 μm, respectively. The minimum grain size 3.47 μm was obtained after 4-pass FSP on CuAl9Mn2 + 10%W samples. The tensile strength of the composites, however, decreased as compared to that of the as-received and FSPed bronze, while microhardness was almost the same number for all samples. The maximum wear resistance was achieved on the 4-pass FSPed sample containing 5 vol.% W.

Keywords copper alloy, friction stir processing, mechanical properties, structure, tungsten, wear

1. Introduction

It is known that adding refractory W particles to the high conductivity Cu matrix allows obtaining composites or pseudoalloys that provide high thermal and electrical conductivity, stability against wear by electric erosion as well as improved mechanical strength. Therefore, such composites may be used to create moving elements of machines and devices, electronic seals, high-voltage electrical contacts, nuclear materials, electromagnetic railway hardware, nozzle throats for rocket engines and oval hole guides for the precision rolling mills, for electromagnetic gun rails and precision guides for rolled pieces of warheads, heat sink materials and deviator plates for fusion engines due to their good ablation resistance and electrical conductivity (Ref 3-5). Such a wide range of applications of W/Cu pseudoalloys is due to the high-temperature hardness of W at high temperatures and its high melting point W, as well as the ability of these pseudoalloys to generate antifriction layers at different operating temperatures (Ref 6). In addition, the frictional heat generated during sliding can be quickly removed due to the high thermal conductivity of the copper matrix that allows reducing the surface temperatures and, therefore, prolong the service life of engineering structure components (Ref 7).

A number of methods could be used for fabricating the W/Cu composites with the majority of them relating to consolidation of W/Cu powder blends using the powder metallurgy processes (Ref 8-13). An *in situ* reaction strategy had been also proposed for the synthesis of a nanocomposite based on W-Cu co-doped with Cr and WC, so that the obtained multicomponent nanocrystalline volume would have had a homogeneous distribution of various phases (Ref 14). Despite the above mentioned ones, there are many other methods suitable for preparation of copper alloy/W composites. However, obtaining the full-density copper alloy/W composites by means of these methods would be rather difficult, not only because its components such as copper and tungsten are immiscible but also because there are big differences in both thermal expansion and melting temperatures (Ref 16, 17). Another negative factor may be that copper makes too soft matrix in order to provide high mechanical characteristics and sound retention to the W particles as well as copper matrix is not the best choice from the viewpoint of tribology.

On the other hand, bronzes possess good formability, high ductility, electrical and thermal conductivities and corrosion resistance. There properties allow them to be used in various industries including mechanical engineering, electrical engi-

Andrey Cheremnov, Anna Zykova, Nickolai Savchenko, Evgeny Knyazhev, Natalya Semenchuk, Denis Gurianov, Andrey Vorontsov, Veronika Utyaganova, Andrey Chumaevskii, Evgeny Kolubaev, and **Sergei Tarasov**, Institute of Strength Physics and Material Science, Siberian Branch of Russian Academy of Sciences, 634055 Tomsk, Russia. Contact e-mail: tsy@ispms.ru.

Published online: 04 April 2024

neering, automotive industry, etc. (Ref 1, 2). It is also possible to improve these characteristics by alloying (Ref 2). The addition of tungsten particles to bronze can significantly improve both strength and wear resistance of the final composite while still providing high electric and heat conductivities. For instance, tungsten–bronze high-density high-hardness composites have been obtained using encapsulation of W-bronze green powder compacts in bronze powder shells and sintering at 1150 °C (Ref 18). Such a functionalization allowed achieving 97-99% of theoretical density and 1-20% gain in hardness.

Addition of hard particles to a ductile metal matrix by means of friction stir processing is one of the methods for fabricating metallic matrix composites including adding hybrid combinations of reinforcement particles such as Ni and W (Ref 19). Admixing 70 vol.% Ni + 30 vol.% W and 40 vol.% Ni + 60 vol.% W to copper allowed increasing the microhardness of the composite. However, neither reinforcement particle distribution nor quantification of wear was carried out to judge of either composite homogeneity or wear resistance of the MMCs.

The consolidated powders or as-cast composite are prone to have porosity as well as high temperatures and/or fusion-base methods may result in redistribution of other alloying elements and forming phases that would have a deleterious effect on structural and mechanical characteristics of the composite.

Solid-state base intermixing of reinforcement particles into ductile matrix may be achieved using friction sir processing (FSP). Numerous publications are easy to find that have been devoted to FSP preparation and studying of such composites prepared on the base of aluminum and magnesium alloys by intermixing them with SiC, TiC, B_4C, Al_2O_3, SiO_2, NiTi, Al_3Ti, AlFe, etc. particles. The use of multipass friction stir processing (FSP) may be the route to minimize overheating and porosity of the metal matrix reinforced with hard metal particles (Ref 20). The FSP process is carried out at a temperature not higher 0.3-0.8T_m of the matrix's metal melting point and therefore main structure formation processes are determined by strain-induced solid-state dissolution of components and then forming new recrystallized refined solid solutions grains and precipitates of intermetallic compounds (IMC). In some cases, even a liquid phase can be in-situ formed because of exothermic liquation effects (Ref 21, 22). Another important aspect is adhesive interaction between the plasticized metal and FSP tool that can also lead to forming new phases (Ref 23).

Application of friction stir processing for fabrication of a copper-tungsten composite was undertaken by Ahuja et al. (Ref 24) using a probeless (pinless) tool and rectangular tungsten insert in the copper block. In fact, only some mechanical interlocking has been achieved at the copper/tungsten interfaces instead of tungsten dispersion and intermixing.

A Cu-TiC MMC was prepared using FSP on the copper plate with TiC-filled holes (Ref 25). Despite using at least three FSP passes, the distribution of tungsten particles was not homogeneous but, nevertheless, wear reduced by a factor of 5 compared to that of pure copper. The multipass FSP was used also to prepare Cu/SiC composites with improved dispersion of carbide particles and mechanical properties (Ref 26). The major problem with preparation of MMCs by FSP is to provide homogeneous distribution and deagglomeration of powder agglomerates. The multipass FSP may be the most practical method to find a solution to this problem. It was shown using the x-ray μCT (Ref 27) that four passes provided acceptable homogeneity of the powder distribution in the matrix.

Therefore, the purpose of this work is to study structural evolution, phase transformations, and changes in the mechanical properties of the FSPed CuAl9Mn2 bronze and bronze/W composites with different W content, obtained by friction stir processing.

2. Materials and Methods

The CuAl9Mn2 bronze samples were in the form of plates cut off the 2 mm of thickness rolled sheet. This metal was composed of phases such as α-Cu(Al) solid solution and (α + β′)-eutectoid (Fig. 1a). The source tungsten powder particles are shown in Fig. 1(b).

Tungsten powder was loaded into 1.5 mm of depth holes drilled in the bronze plate as shown in Fig. 2(a). The number of holes, their diameter and distance between them were determined to provide the desired volume fraction of the tungsten in the composite stir zone (Table 1).

The designed volume fractions of the tungsten particles in the stir zone corresponded with those obtained from the SEM images of the stir zones sections using the intercept method. Finally, the volume fractions of tungsten were measured as those shown in Table 1 (error is ± 0.5 vol.%).

The FSP was carried out in experimental friction stir welding machine (ISPMS SB RAS, Tomsk, Russia) using either single or four passes in order to study the degree of

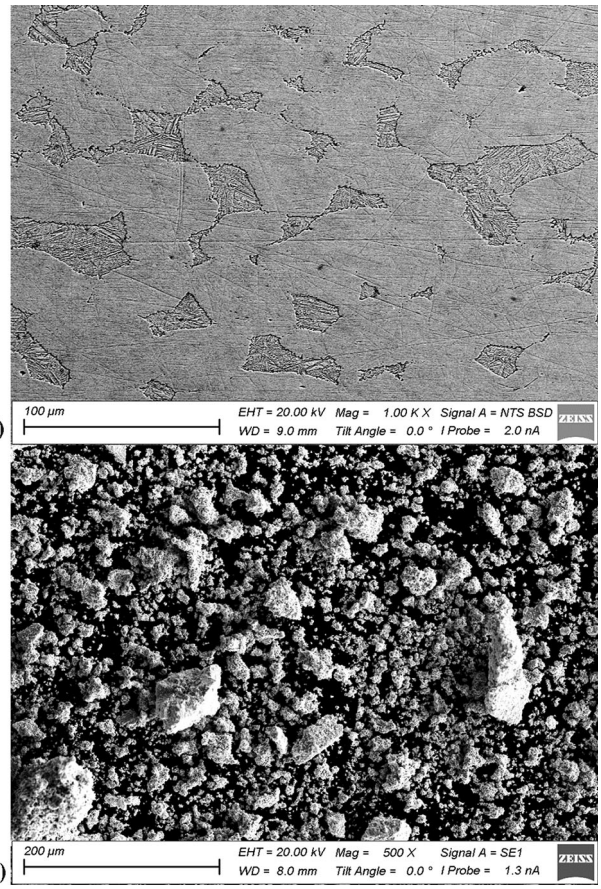

Fig. 1 SEM BSE image of initial CuAl9Mn2 (a) and SEM SE image of W powder particles used in experimenting (b)

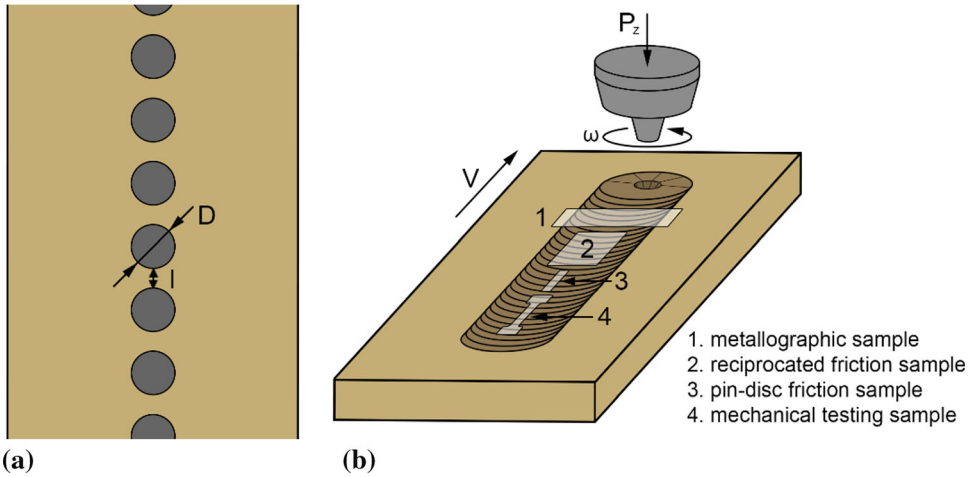

Fig. 2 Holes drilled in the bronze plate and filled with tungsten powder (a), scheme of FSP and sampling from the stir zone (b)

Table 1 Diameter of holes, distance between them and measured tungsten powder contents depending on the designed tungsten content in the composite

W, vol.%	D, mm	l, mm	vol.% W after 1-pass FSP	vol.% W after 4-pass FSP
5	1.5	4.9	5.06	5.04
10	2.0	4.7	5.05	4.96
15	2.5	4.7	5.02	4.99

intermixing and its effect on structural and mechanical evolution of the samples resulting. The FSP tool was made of WC/15Co hard metal and had a tapered cone 1.9 mm of height pin (Fig. 2b). The process parameters (Table 2) were obtained from a row of preliminary experiments.

Samples intended for mechanical testing and structural examination were machined from the stir zones using an EDM machine DK7750 (Suzhou Simos CNC Technology Co., Ltd. Suzhou, China) (Fig. 2b). The size of the samples was 20 mm × 5 mm × 2 mm. The surface of the samples was subjected to grinding on abrasive paper of various grain sizes, polished with diamond paste, and subsequent etching in a solution of 10 ml HCl + 1 g $FeCl_3$ + 20 ml H_2O. The macrostructure and microstructure were examined using an Altami MET1-C optical microscope (Altami Ltd., Saint Petersburg, Russia), an Olympus LEXT OLS4100 confocal laser scanning microscope (Olympus Corporation, Tokyo, Japan), scanning electron microscopes (SEM) Carl Zeiss LEO EVO 50 (Carl Zeiss AG, Oberhochen, Germany) with Oxford Instruments x-ray energy-dispersive microanalysis attachment and JEOL JEM-2100 transmission electron microscope (JEOL Ltd., Akishima, Japan). The grain size was determined according to the intercept method.

The phase composition of FSP-ed samples was studied using a DRON-7 diffractometer (Bourevestnik, Saint-Petersburg, Russia) with CoKα radiation. Phases formed on the worn surface in tribological testing were detected using DRON-8N x-ray diffractometer (Bourevestnik, Saint-Petersburg, Russia) with grazing-incidence x-ray diffraction, at beam (Cu-Kα) incidence angles of 9°, 6°, 3° with the x-ray penetration depths from ~ 1.3 to ~ 7.8 μm depending on the composition of the samples. The penetration values were calculated in accordance with (Ref 28).

Table 2 Process parameters used for both single-pass and four-pass FSP

V, mm/min	*ω*, rpm	P_{load}, kg	$P_{z.}$, kg
150	500	1000	900

To assess their mechanical properties, samples were cut out in the form of dog-bone specimens with total length of 23 mm, their gauge length, width and thickness were 12 mm, 3 mm, and 2 mm, respectively. The samples were then tested by means of on a universal testing machine UTS 110 M-100 (Testsystems, Ivanovo, Russia). The measurement of microhardness values was carried out using an AFFRI 8 microhardness tester (Affri, Italy) (step 0.5 mm, load 500 g, measurements were taken along the length of the sample at equal distances from the edges of the sample).

Tribological tests were carried out without the use of lubricants with sliding direction oriented across the FSP direction according to the "pin-on-disk" scheme. The tests were carried out using a TRIBOtechnic tribometer (Tribotechnic, Clichy, France) on samples 10 mm × 2 mm × 2 mm in size. The test parameters were as follows: the ∅30-mm disks made of quenched and tempered AISI 52100 steel rotated at 250 RPM (0.26 m/s) while pins were pressed to them by the normal force F = 15 N for 2 h.

3. Results

3.1 XRD of Bronze and Bronze/W

Figure 3 shows x-ray diffraction patterns obtained from an as-received bronze sample as well as from stir zones (SZ) formed by either single-pass or four-pass FSP. All the samples are characterized by the presence of α-Cu and β′-phases. The angular positions and intensity ratio of α-Cu solid solution reflections did not change depending on the number of FSP passes (Fig. 3). However, some slight decrease of the β′-phase peaks' heights can be observed that testifies on reducing the volume fraction of this phase depending on the pass number.

On admixing 5 vol.%, 10 vol.% and 15 vol.% W into CuAl9Mn2 with either 1 or 4 FSP passes, the SZs contain phases such as α-Cu, β′-Cu_3Al, γ-Al_4Cu_9 and W (Fig. 4). At the same time, no differences are observed in the x-ray diffraction patterns as-depended on the W concentrations and the number of FSP passes. The semi-quantitative analysis of the XRD peak intensities allows observing how concentrations of the constituent phases change in the thin subsurface layers of the composites. These changes look as negligible even for α-W whose designed volume content increased from 5 to 15 vol.% content. The possible explanation may be that x-ray penetration into the composites was comparable to those of W particles and, therefore, almost the same number of them was contained within the x-ray penetration layer.

Semi-quantitative XRD peak height analysis allowed also determining the relative contents of phases, mainly Cu_3Al and Al_4Cu_9 in the composites as depended on the percentage of W and number of FSP passes (Fig. 4c). It can be observed that the contents of Al_4Cu_9 is almost constant for all composites with slight tendency for reduction at 15 vol.% W. The percentage of Cu_3Al in the 15 vol.% W composite is a bit higher which may be the result of inhibiting the $\beta \rightarrow \gamma + \alpha$ transformation by tungsten.

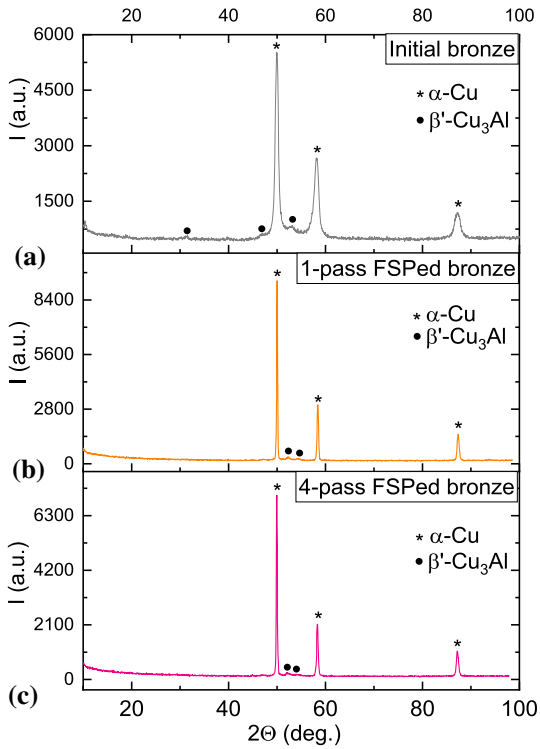

Fig. 3 XRD patterns of as-received CuAl9Mn2 (a), 1-pass FSPed (b) and 4-pass FSPed manganese aluminum bronze (c)

3.2 Structure Analysis of CuAl9Mn2 after FSP

The optical and scanning electron microscopy studies show that a macrostructure typical for FSPed samples (Fig. 5 and 6) and represented by the nugget zone or stir zone (SZ), thermo-mechanically affected zone (TMAZ), heat affected zone (HAZ), and base metal (BM) has been formed. The boundaries between SZ and TMAZ are also typical: on the retreating side (RS) the boundary is blurred, while on the advancing side (AS) there is a clear line between them. At the same time, the HAZ are hardly distinguishable on the macrostructure views. This macrostructure type is typical for the samples obtained after one and four FSP passes. The base metal of the CuAl9Mn2 alloy is represented by large grains, the size of which varies from 53 to 107 μm.

Figure 5a shows the macrostructure of the SZ formed by the single–pass FSP wherein the equiaxed shape of the grains prevail in the top SZ region closer to RS, (Fig. 5b, c), while in the rest of the SZ volume, the grains have a slightly elongated shape (Fig. 5d) with the grain size from 1.5 to 8.2 μm (Fig. 7).

Figure 7 shows the macrostructures and microstructures formed in the CuAl9Mn2 after 4 FSP passes. The bronze grains in SZ became almost equiaxed through the entire volume of the stir zone. The structure here is visually more uniform than that in a sample obtained with a single FSP pass. The grain size in SZ ranges from 2 to 6 μm. In the TMAZ, the grains are elongated in the direction of tool movement during processing (Fig. 6d). At the same time, the grain size decreased to 17 ÷ 40 μm.

Using the TEM examination it was found that dynamically recrystallized grains of the CuAl9Mn2 solid solution with annealing twins and stacking faults are formed in SZ after 4 FSP passes (Fig. 8a–c). An eutectoid structure can be observed also along the boundaries of the recrystallized CuAl9Mn2 grains (Fig. 8c, j). Identification of the SAED pattern in Fig. 8d allows observing the presence of γ-Al_4Cu_9 phase in the form of martensitic (bainitic) laths as well as in the form of spherical particles inside the α-Cu grains (Fig. 8c–f). It is not inconceivable that these bainitic laths belong to γ′-Al_4Cu_9. The (α + β′) eutectoid is located along the α-Cu grain boundaries (Fig. 8j–i).

3.3 Structure Analysis of CuAl9Mn2 with 5 vol.% W after FSP

Figure 9 and 10 shows the macrostructural and microstructural views, respectively, of the CuAl9Mn2 alloy samples admixed with 5 vol.% W after 1-pass FSP. The SZ and TMAZ in the AS have macrodefects in the form of discontinuities (Fig. 9a and 10). Some W particle aggregates can be observed in subsurface of SZ, as well as on the AS, which may be indication of insufficient intermixing after 1-pass FSP (Fig. 9a, c, d). The grain size of α-Cu in SZ after 1-pass FSP is from 2.6 to 12.8 μm (Fig. 10), which is slightly larger than that after FSP on the as-received bronze. Generally, the presence of large regions (Fig. 10) with concentrated W-particles demonstrates that 1-pass FSP is insufficient for providing their homogeneous distribution.

The 4-pass FSP of the bronze/5vol.%W samples resulted in a more homogenous distribution of the W powder in the SZ that allowed also to eliminate the discontinuities (Fig. 11 and 12). In

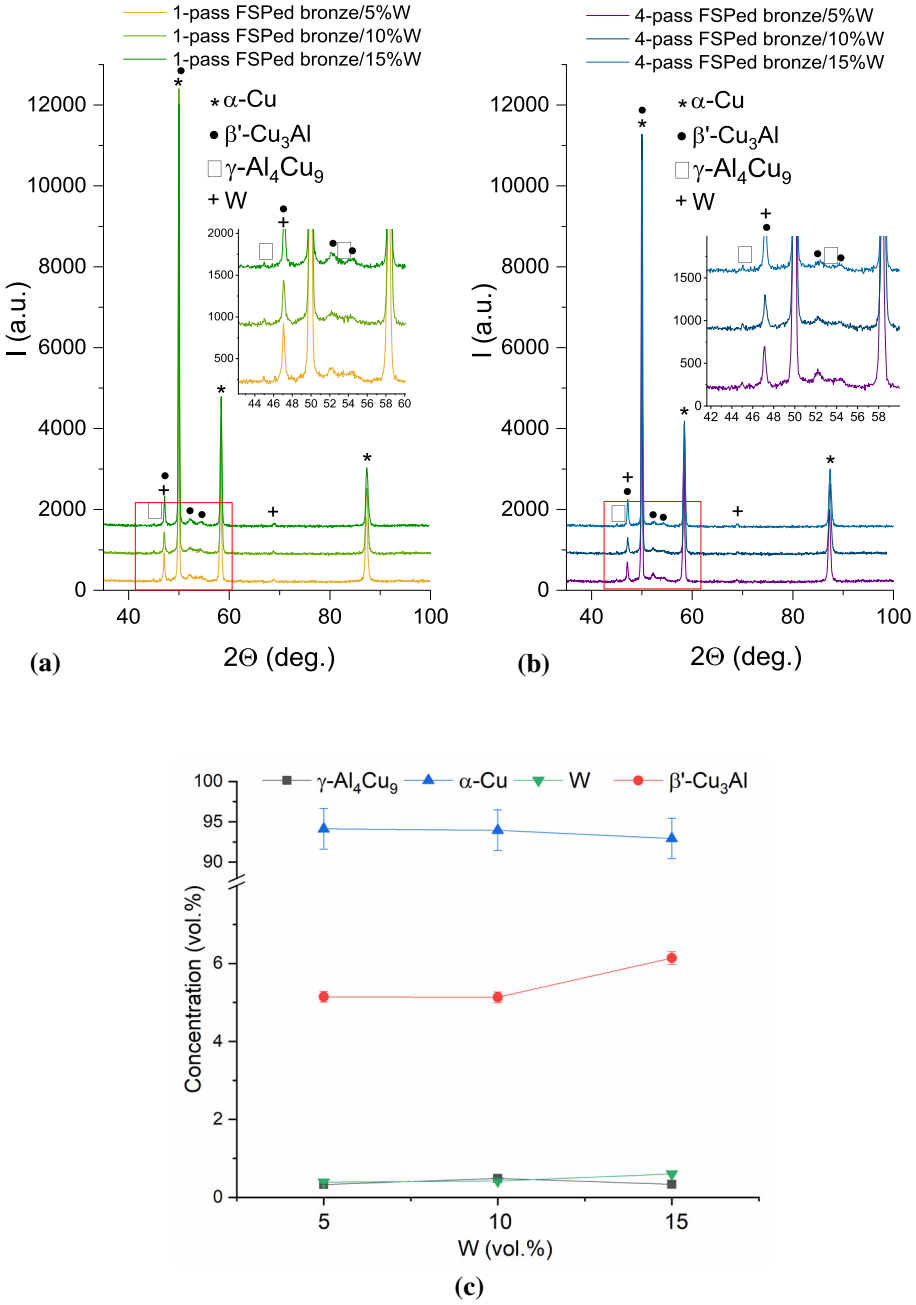

Fig. 4 XRD patterns of CuAl9Mn2/W composites after 1-pass FSP (a) and 4-pass FSP (b). Volume fractions of phases in the 4-pass FSPed composites vs. percentage of W (c)

this case, the grain size of CuAl9Mn2 SZ ranged from 1.9 to 10.9 μm, i.e., decreased compared to that after the 1-pass FSP (Fig. 12). The microstructure of CuAl9Mn2/5vol.%W after 4-pass FSP shows isolated W particles on the background of bronze grains (Fig. 12).

The admixing of 5 vol.% W into CuAl9Mn2 does not lead to any changes in the structural-phase state of SZ (Fig. 13). Just as in the samples without any powder addition, dynamically recrystallized CuAl9Mn2 grains with annealing twins are observed (Fig. 13a, b). The (α + β')-eutectoid is localized along the α-Cu grain boundaries (Fig. 13b, c, e, f). The presence of the β'-phase is indirectly confirmed by the data of EDS analysis, according to which this phase contains $\sim$ 24.6 at.% Al and $\sim$ 73 at.% Cu (Fig. 13b, spectrum 4, Table 3). The nanosized β'-particles are also observed in the grains of the α-Cu solid solution near the boundaries with the eutectoid, which is confirmed by the dark-field image obtained in the reflection $(0\bar{2}2)_{\beta'}$ (Fig. 13b, e). In addition to the β'-phase particles, there are ones inside the α-Cu grains that were enriched with W (Fig. 13b, spectra 2-3, Table 3).

According to the EDS elemental maps, W particle aggregates of various sizes are found on the α-Cu grain boundaries (Fig. 14).

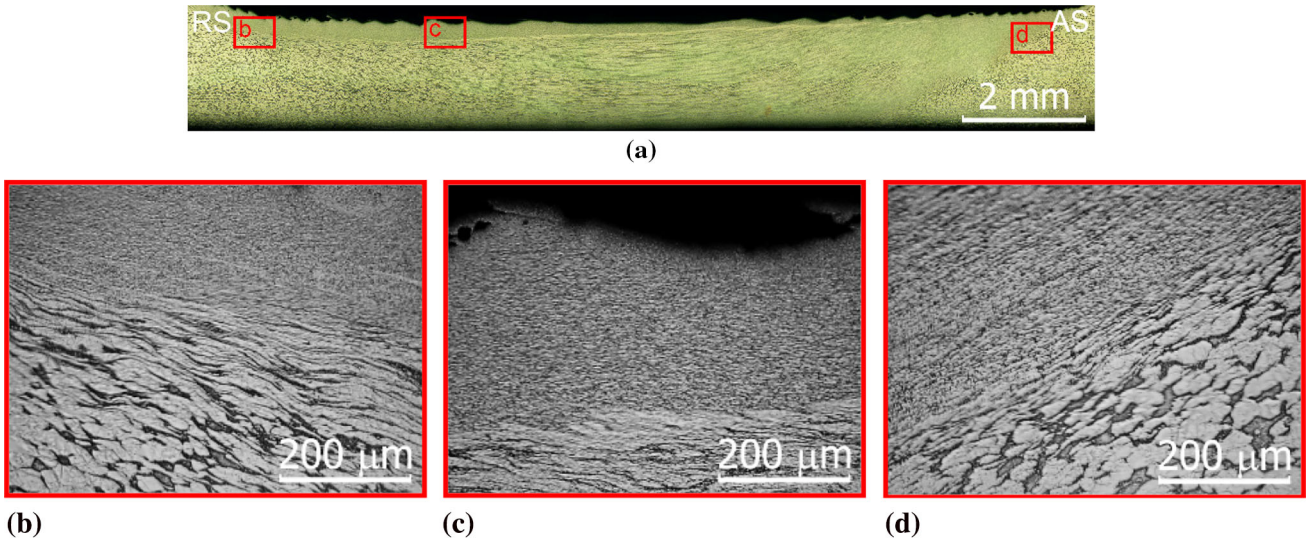

Fig. 5 Macrostructure of CuAl9Mn2 after 1-pass FSP (a) and microstructures at the SZ/TMAZ boundary closer to RS (b), in SZ (c), and at SZ/TMAZ boundary closer to AS (d)

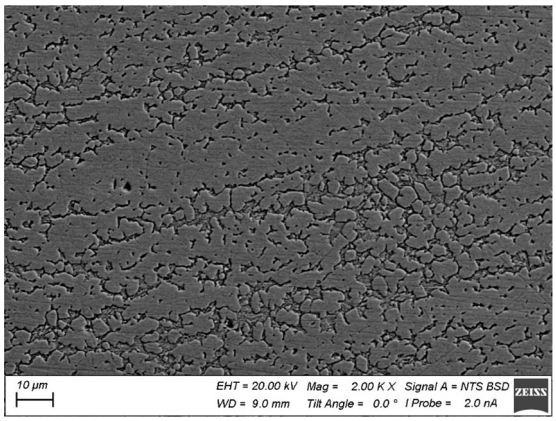

Fig. 6 SEM BSE microstructure image of CuAl9Mn2 after 1-pass FSP

3.4 Structure Analysis of CuAl9Mn2 with 10 vol.% W after FSP

Similarly to the previous samples, adding 10 vol.% W into CuAl9Mn2 with a single-pass FSP has led to discontinuities and inhomogeneous distribution of W powder on the advancing side of the SZ (Fig. 15a, c, d, 16). These defects were eliminated with the 4-pass FSP (Fig. 17 and 18). The grain sizes in the SZ of the bronze/10%W sample after 1-pass and 4-pass FSP were 1.4 ÷ 11.5 μm (Fig. 16) and 1.3 ÷ 10.9 μm (Fig. 18), respectively, which is comparable to that found in the above-discussed bronze/5 vol.% W sample.

3.5 Structure Analysis of CuAl9Mn2 with 15 vol.% W after FSP

Elongated with the FSP material flow pattern discontinuities were formed in a composite containing 15 vol.% W in

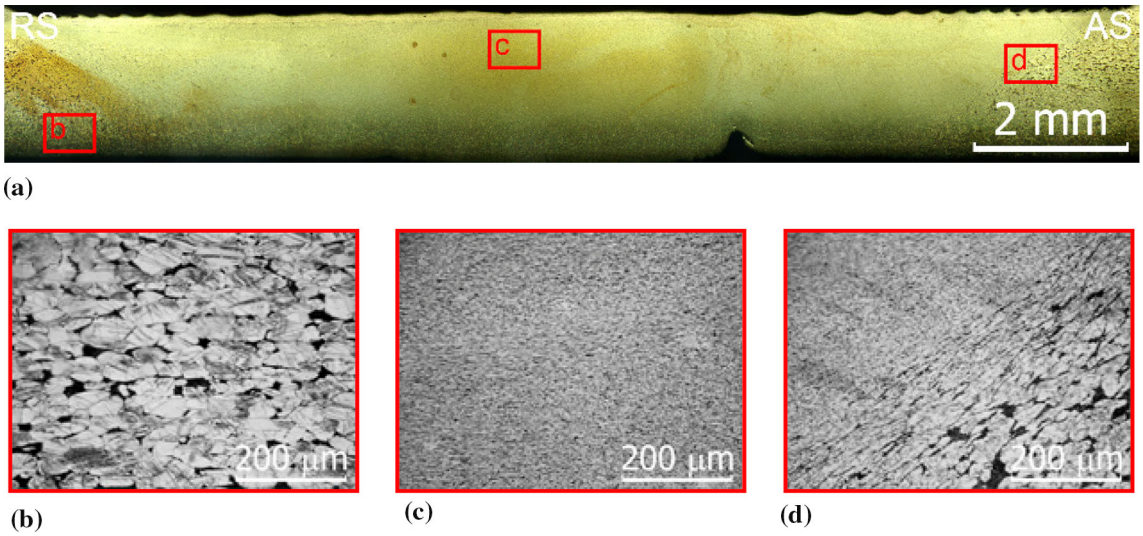

Fig. 7 Macrostructure of CuAl9Mn2 after 4-pass FSP (a) and microstructures at the SZ/TMAZ boundary closer to RS (b), in SZ (c), and at SZ/TMAZ boundary closer to AS (d)

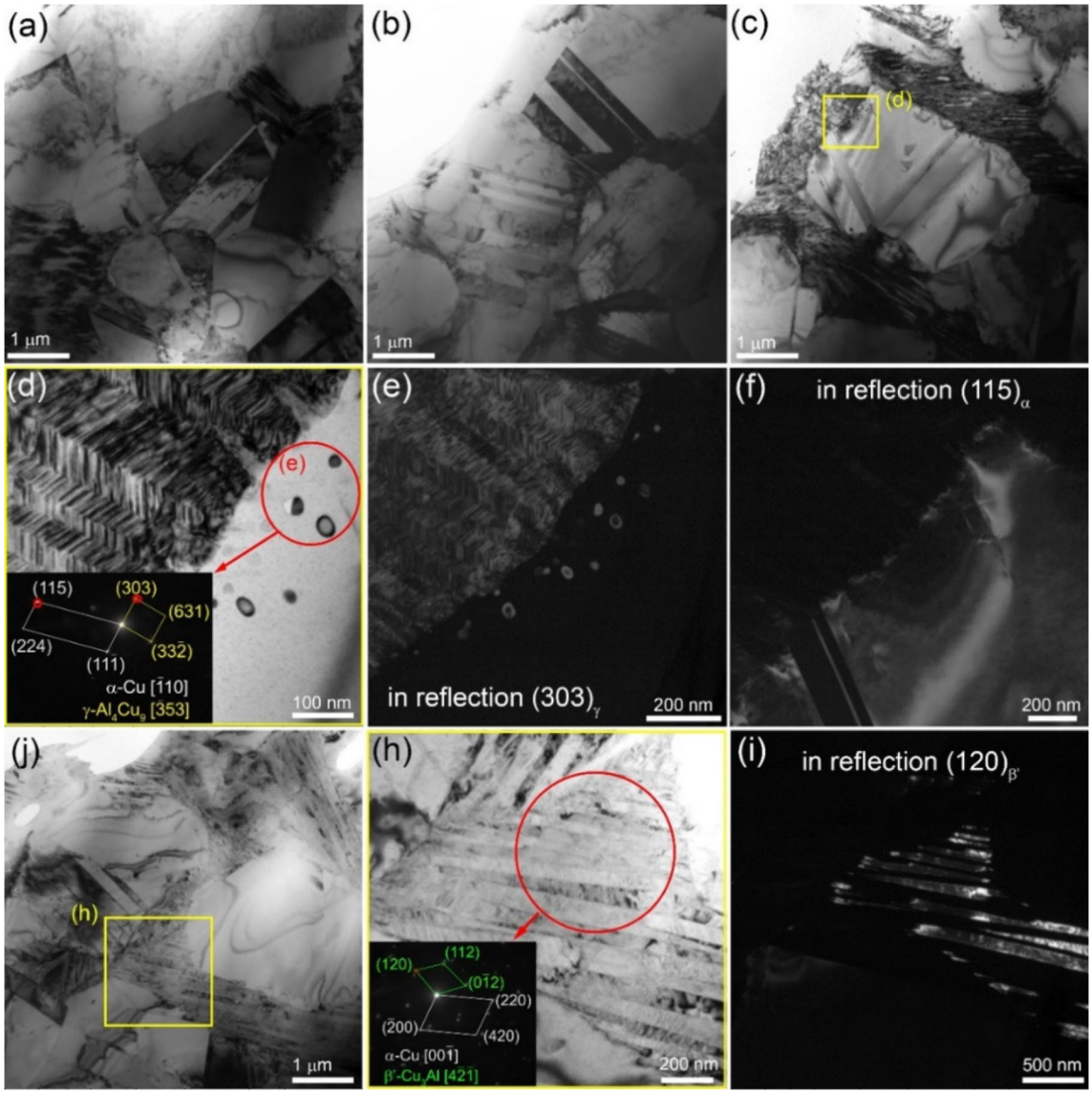

Fig. 8 Bright-field TEM images of CuAl9Mn2 of structures formed in SZ after 4-pass FSP (a–d, j, h), dark-field TEM images (e, f) obtained using reflections $(303)_\gamma$ and $(115)_\alpha$ from zone in (d) images and dark–field image (i) obtained using reflection $(120)_{\beta'}$ from zone in (h)

CuAl9Mn2 matrix after 1-pass FSP (Fig. 19a, d), which have then been eliminated using the 4-pass FSP (Fig. 20). More tungsten powder was concentrated in the bottom (root) part of the SZ as compared to its other parts (Fig. 20a–c). The grain size in the SZ of the bronze/15 vol.% W sample after 1 and 4 FSP passes is identical, i.e., 1.3 ÷ 14.1 μm (Fig. 21 and 22), which is comparable to the grain sizes found in previously examined samples containing tungsten powder.

A more detailed study of the SZ using the TEM method showed that the W particle aggregates were unevenly distributed in the SZ and had different sizes (Fig. 23a–c). Similar to the previous samples, the large number of annealing twins can be observed in the recrystallized α-Cu grains (Fig. 23a–c, d, f, g). The (α + β')-eutectoid grains are localized along the α-Cu grain boundaries, as confirmed by corresponding dark-field images obtained in reflections identified on the SAED pattern (Fig. 23a, e–i). According to EDS maps, the β'-Cu_3Al phase consists of 17.9 at.% Al and 77.7 at.% Cu (Fig. 24, spectrum 6, Table 4).

The SZ contains γ-Al_4Cu_9 particles, which, according to EDS analysis, contain up to 29.2 at.% Al and 66.6 at.% Cu (Fig. 24, spectra 1-3, Table 4). Small amounts of tungsten can be also observed in these particles (Table 4, spectra 1-2). The SAED pattern in Fig. 24b does not show any signs of either IMCs or oxides near the W particles which are localized both inside the α-Cu grains and on the grain boundaries (Fig. 23a–b, Fig. 24 b). According to EDS, the insignificant amounts of both Fe and Cr are there whose presence may be associated with the presence of steel wear debris from drilling the holes.

The mean sizes of CuAl9Mn2 grains and W particles asdepended on the content of W and the number of passes FSP are shown in Fig. 25. The more FSP passes, the smaller are both α-Cu and α-W grains. It is obvious that more intensive stirring serves for more effective deagglomeration of the tungsten particles but, in addition, there may be a slight tendency for reducing the W particle size with increasing the content of the tungsten loaded. Such an effect may be provided

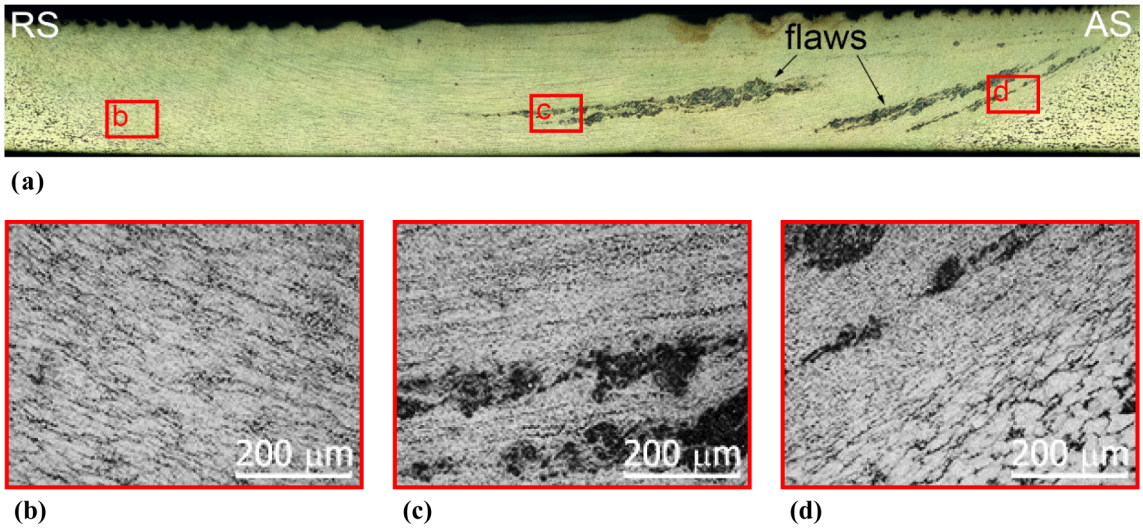

Fig. 9 Macrostructure of CuAl9Mn2/5%W after 1-pass FSP (a) and microstructures at the SZ/TMAZ boundary closer to RS (b), in SZ (c), and at SZ/TMAZ boundary closer to AS (d)

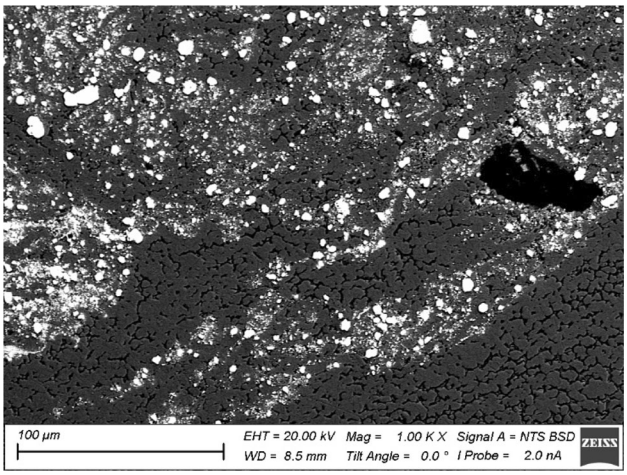

Fig. 10 SEM BSE microstructure images of W-enriched regions in CuAl9Mn2/5%W after 1-pass FSP

by increased stiffness of the composite and therefore more effective crushing of the agglomerates.

3.6 Microhardness and Mechanical Properties

The distribution of microhardness numbers correlates well with the location of structural zones on the optical macroimages. The zone boundaries are clearly visible by the reduced microhardness TMAZ on both AS and RS (Fig. 26) and higher hardness of SZ as compared to average microhardness of the base metal at the level of 1.59 GPa. After the first pass, the average value of microhardness in TMAZ is 1.66 GPa, in SZ it is 1.70 GPa. After the fourth pass, the microhardness values in TMAZ are 1.77 GPa and in SZ are 1.85 GPa (Fig. 26a).

The addition of tungsten particles slightly reduced the average microhardness values, even as compared to those of the as-received bronze. Thus, the average values of microhardness in 1-pass FSPed samples added with 5 vol.%, 10 vol.%, and 15 vol.% W are 1.63 GPa, 1.58 GPa, and 1.52 GPa, respectively; in TMAZ, they are 1.60 GPa, 1.56 GPa, and 1.37 GPa, respectively. After four FSP passes, the average microhardness values of the samples with 5%, 10%, and 15% alloying material are 1.69 GPa, 1.67 GPa, and 1.75 GPa, respectively; in TMAZ, they are 1.65 GPa, 1.53 GPa, and 1.47 GPa, respectively. The microhardness reaches values greater than that of the tungsten-free bronze, only in case of indenting the W aggregate layer in a sample with 15 vol.% W after 4-pass FSP. The average value of microhardness in this layer is 1.96 GPa (Fig. 26b).

Before processing, the CuAl9Mn2 alloy showed values of tensile strength (σ) and yield strength ($\sigma_{0.2}$) at the levels of 635 MPa and 498 MPa, respectively. Even after the 1-pass FSP these characteristics increased to 743 MPa and 578 MPa, respectively. The 4-pass FSP served, however, to slightly reducing them to 740 MPa and 501 MPa, respectively (Fig. 27b, c).

The addition of tungsten particles served to reducing both the ultimate strength and yield strength values. The addition of 5 vol.% W and one pass of FSP reduced the tensile strength to 477 MPa and the yield strength to 329 MPa. Increasing the number of FSP passes to four increased the tensile strength and yield strength to 580 MPa and 387 MPa, respectively. The addition of 10 vol.% W to bronze and one FSP pass reduced the tensile strength and yield strength to 371 MPa and 303 MPa, respectively, four FSP passes increased the tensile strength to 616 MPa, and the yield strength to 389 MPa. Adding 15 vol.% W slightly increased the tensile strength and yield strength after one FSP pass to 389 MPa and 321 MPa, respectively. Four-pass FSP bronze with 15 vol.% W changed the tensile strength to 539 MPa, the yield strength to 394 MPa (Fig. 27b, c). The tensile curves of the samples are shown in Fig. 27a.

SEM BSE images of the tensile test fracture surfaces of the 1-pass FSP-ed bronze/W samples after 1 passes showed that W particle aggregates are only negligibly bonded to the bronze matrix so that macrocracks are formed along these aggregates and samples is fractured into large fragments (Fig. 28a, 29a, 30a). At the same time, the fractographic analysis of the 4-pass FSP-ed bronze/W samples showed that the W particulates are present on the ductile fracture surface consisting of ridges and dimples (Fig. 28b, 29b, and 30b). The dimples were formed by pulling out ductile bronze metal around the hard non-deformed

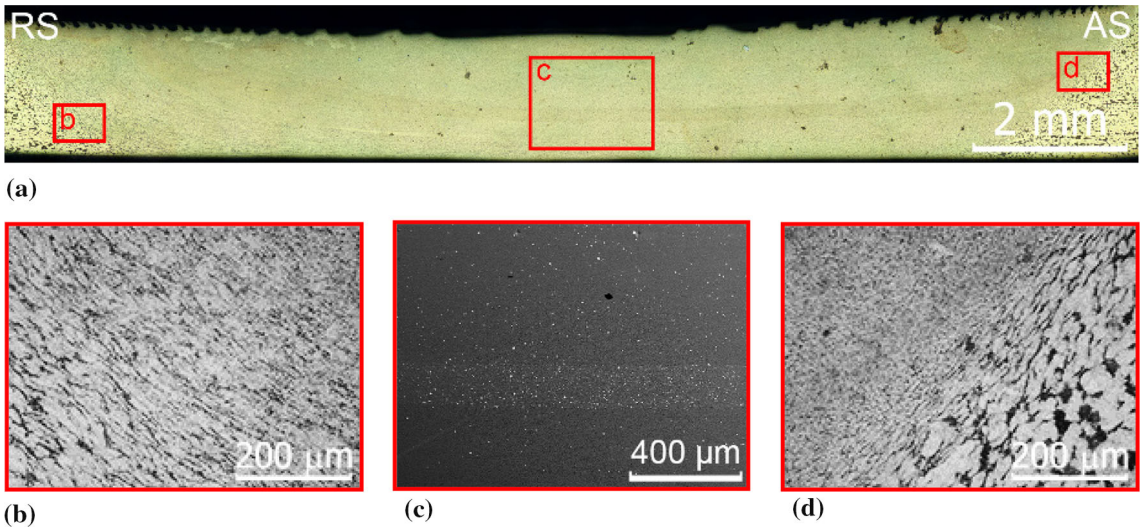

Fig. 11 Macrostructure of CuAl9Mn2/5%W after 4-pass FSP (a) and microstructures at the SZ/TMAZ boundary closer to RS (b), in SZ (c), and at SZ/TMAZ boundary closer to AS (d)

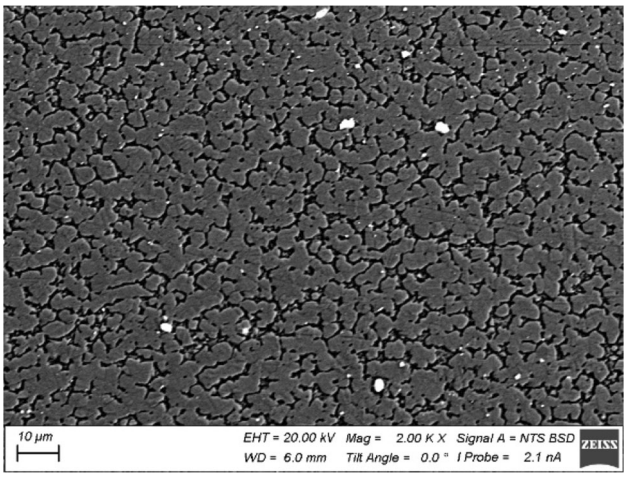

Fig. 12 SEM BSE microstructure images of CuAl9Mn2/5vol.%W after 4-pass FSP.

particles. Those are W particulates almost homogeneously distributed in the bronze matrix.

3.7 Tribological Characteristics

The results of tribological tests are highly dependent on the direction of sliding with respect to FSP tool travel direction. The FSP of as-received bronze subjected to dry sliding tests according to the "pin-on-disk scheme (Fig. 31) allowed reducing the average value of the coefficient of friction (CoF) on samples after both 1-pass and 4-pass FSP.

The CoF values after four FSP passes slightly increased compared to that of 1-pass FSP pass, while wear significantly reduced as compared to that of the FSPed bronze samples. The change in the values of the friction coefficient during testing of a single-pass sample occurs unevenly: for example, after 1000 s of testing, the average value of the friction coefficient decreases while the scatter of values during testing increases (Fig. 31a).

The addition of tungsten to the composite increased the average coefficient of friction. At the same time, in the process of testing a composite with 5 vol.% W after one FSP pass, the values of the CoF were changing greatly from values close to the that of sample without tungsten to the values of corresponding to those of obtained after 4-pass FSP on the 5 vol.% W sample. It was the sample with the highest CoF value and, at the same time, the lowest wear. The CoF on samples with 10 and 15 vol.% W did not noticeably differ from each other. Also, the number of FSP passes used for preparing the samples with 10 vol.% W did not noticeably change the tribological properties, while for samples with 15 vol.% W there were some differences in the CoF values (Fig. 31b–d). The four-pass sample, as compared to the others, showed slightly worse properties at the beginning of the test, and the one-pass sample at the end (Fig. 31a).

The behavior of wear assessed by the linear dimensions of the samples (Δl) and by their mass losses (Δm) showed the same type of behaviors as shown in Fig. 31c, d. The Δl wear of W-containing samples reduced and increased as compared to that of 1-pass FSPed bronze and as-received bronze. This increasing was the most notable in case of testing the 10 vol.% W sample. The 4-pass FSPed W-containing samples showed wear higher than that of the FSPed bronze with the exception of wear on the 5 vol.% W sample. The Δm wear of the W-containing samples was always lower compared to that of the FSPed and as-received bronze irrespective of the FSP pass number (Fig. 31d).

The results of structural studies of the worn surfaces of the FSP-ed bronze samples and bronze/W samples after tribological testing according to the "pin-on-disk" scheme are given below.

3.8 XRD of Bronze and Bronze/W after Tribological Testing

The GIAXRD pattern was obtained using the beam incidence angle 3° from the worn surface of the 4-pass FSPed sample (Fig. 32) that demonstrated the presence of the base metal phases α-Cu, β′-Cu_3Al as well as additional phase Cu_4Al that appeared after sliding in air. Deeper x-ray penetration that was achieved using the incidence angles 6° and 9° allowed identifying α-Cu, β′-Cu_3Al and α-Cu, β′-Cu_3Al, γ-Al_4Cu_9, respectively. The subsurface layers of the composite containing 5 vol.% W showed the presence of κ-Al_2O_3 phase in addition

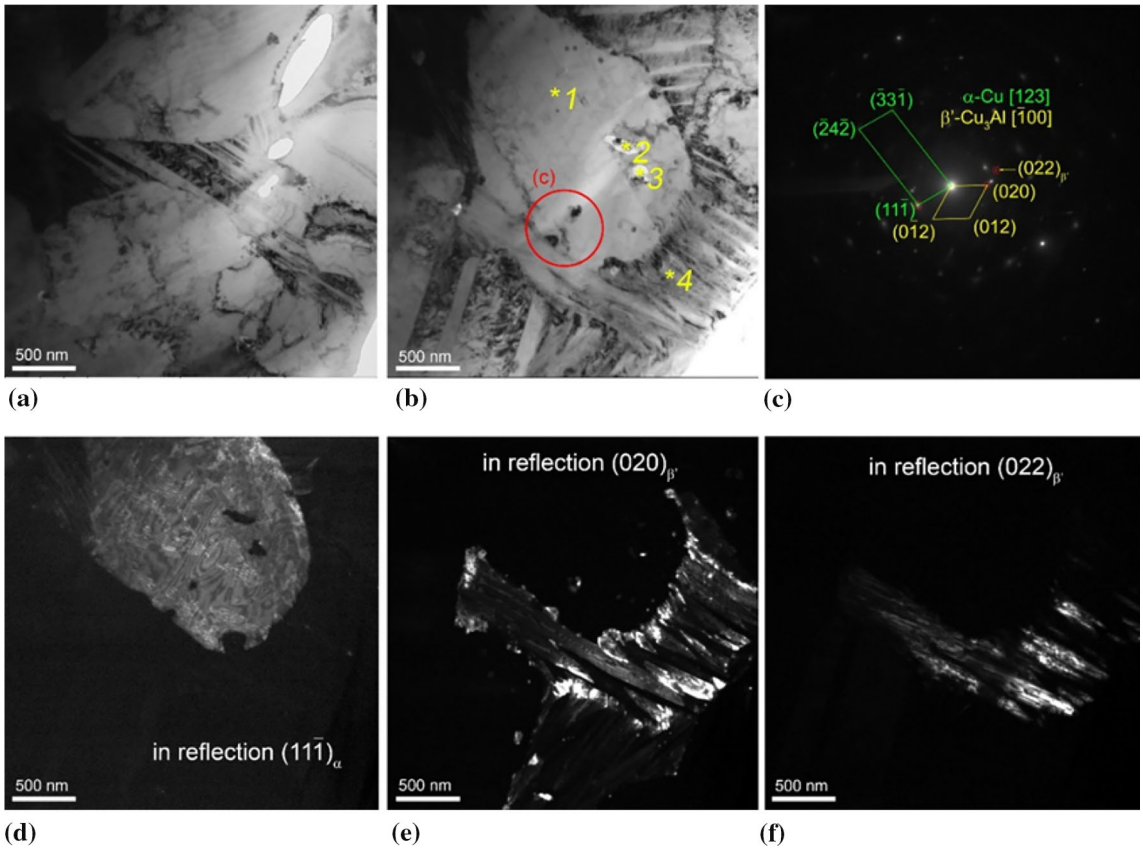

Fig. 13 Bright-field TEM images of microstructures in SZ of bronze/5 vol.%W after 4-pass FSP (a, b), SAED pattern from the zone (c) inside the red circle, dark-field TEM images (d–f) obtained using reflections $(11\bar{1})_{\alpha}$, $(020)_{\beta'}$ and $(022)_{\beta'}$

Table 3 EDS spectra from the SZ of FSPed bronze/5%*W* (Fig. 13b)

	Content, at.%				
Spectrum	**Al**	**Mn**	**Fe**	**Cu**	**W**
1	16.9	0.7	…	82.4	…
2	56.0	6.0	…	30.8	7.1
3	43.4	18.8	8.5	22.3	7.0
4	24.6	2.4	…	73.0	…

to α-Cu, β'-Cu_3Al, γ-Al_4Cu_9, Cu_4Al and α-W. Almost no Cu_4Al was found in the subsurface layer of the composites containing 10 and 15 vol.% W as well as the intensity of κ-Al_2O_3 peak is reduced with the percentage of tungsten. This may mean that tribooxidation of γ-Al_4Cu_9 becomes less intensive in the presence of α-W. It can be suggested that tungsten may be preferably oxidized instead of the matrix components. However, no traces of tungsten oxides have been detected by means of XRD.

The appearance of new phases Cu_4Al and κ-Al_2O_3 has been provided by tribooxidation of the composite matrix composed of α-Cu(Al), β'-Cu_3Al and γ-Al_4Cu_9. Mainly it was tribooxidation of Al and transformation of α-Cu(Al), Cu_3Al or γ-Al_4Cu_9 into Cu_4Al with less atomic concentration of aluminum. It is known (Ref 29) that the γ-Al_4Cu_9 is not a stable compound and easily decomposes into Al and Cu at elevated temperatures. Therefore, it is more plausible that this compound is oxidized favorably in sliding rather than more stable β'-Cu_3Al and α-Cu(Al). The fact that no γ-Al_4Cu_9 was found on the worn surface of the pure bronze at the minimal incidence angle 3° may mean that it was fully converted into Cu_4Al by tribooxidation despite the reaction product κ-Al_2O_3 was not detectable.

3.9 Morphology of the Worn Surfaces

The SEM BSE images of worn surfaces samples (Fig. 33) show that the predominant wear mechanism was the abrasive wear with the formation of grooves due to micro-ploughing. Delaminated layers in the form of craters indicate local adhesive wear. Local agglomerations of the oxidized wear products and abrasive particles can be observed Ha worn

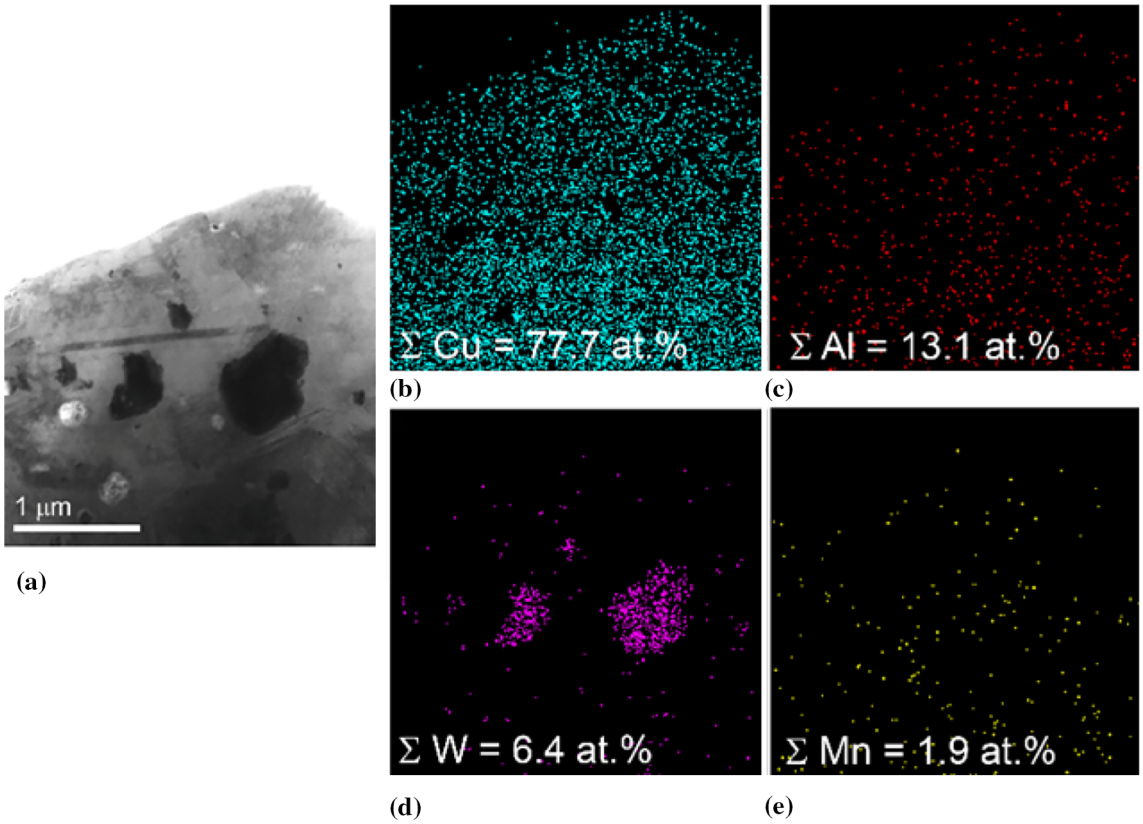

Fig. 14 Bright-field TEM images of small W-aggregates in the bronze/5 vol.%W after 4-pass FSP (a) and corresponding EDS maps (b-f)

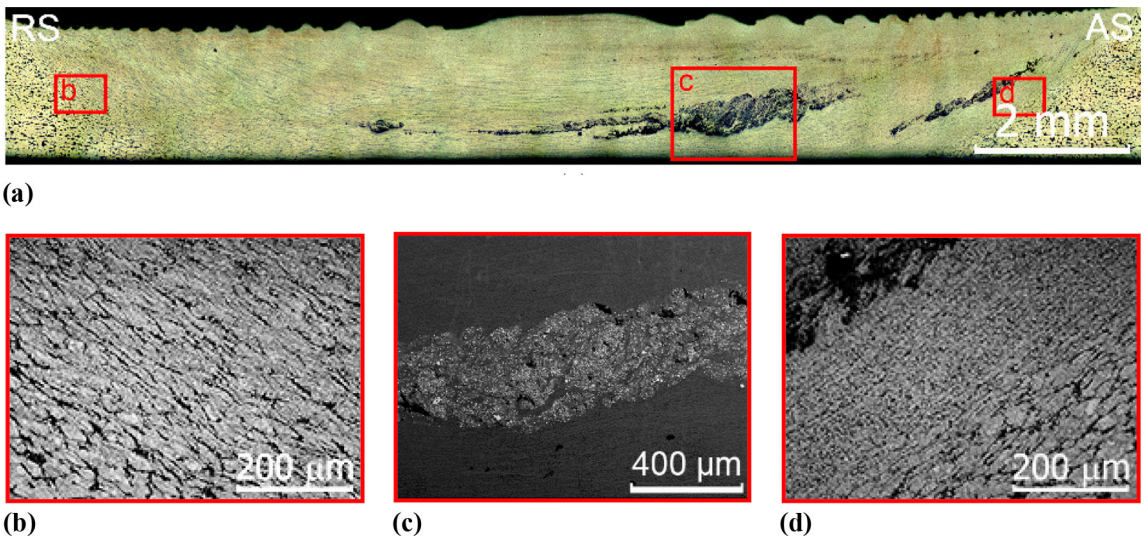

Fig. 15 Macrostructural optical image of structures formed in CuAl9Mn2/10%W by 1-pass FSP (a) and microstructures at the SZ/TMAZ boundary closer to RS (b), in SZ (c), and at SZ/TMAZ boundary closer to AS (d)

surfaces FSP-ed bronze/W samples (Fig. 33b–d) that may then form mechanically mixed layers. The worn surface of all samples contained dark MML with high percentage of oxygen (Fig. 33a, areas 3, 4, Fig. 33b, areas 7, 8, Fig. 33c, areas 11, 12, Fig. 33d, areas 15, 16, Table 5). At the same time, with an increase in the amount of tungsten added during FSP, the amount of oxygen in MML decreased (Fig. 33a, areas 3, 4, Fig. 33b, areas 7, 8, Fig. 33c, areas 11, 12, Fig. 33d, areas 15, 16, Table 5). Surprisingly, there was no iron on the worn surfaces of samples (Table 5), despite the fact that the samples were sliding on the steel counterpart. This could be interpreted, as that generation of mechanically mixed layers does not involve transfer of elements from the steel counterpart.

Subsurface section views demonstrated that MMLs have viscous flow attributes, while if MML of the FSP-ed bronze was characterized by delamination and the formation of multiple defects (Fig. 34a), then for FSP-ed bronze/W composites something like a defect-free quasi-viscous multilayer

subsurface structure was generated (Fig. 34b–d). A striking attribute of such structures were tungsten carbide grains severely deformed along the sliding direction (Fig. 34e–g). The MML contain a significant amount of oxygen (Fig. 34a, areas 1,2, Fig. 34b, areas 5,6, Fig. 34c, areas 9,10, Fig. 34d, areas 13,4, Table 6) and, as previously noted for the worn surface, the amount of oxygen in MML decreased as the amount of tungsten increased. Such a finding is in agreement with the above-made suggestion that the bronze matrix oxidation is inhibited in the presence of tungsten.

4. Discussion

4.1 Microstructures and Phases after FSP

The as-received manganese aluminum bronze was composed of coarse α-Cu and β'-Cu_3Al grains. Severe plastic deformation at elevated temperatures served for full dissolution of the β'-Cu_3Al in α-Cu(Al). On layer-by-layer transfer of the plasticized α-Cu(Al) to the rear zone behind the FSP tool, this metal experienced recrystallization and decomposition into α-Cu and β-Cu_3Al. The latter may then transform into β'-Cu_3Al due to high cooling rates. Despite the fact that no Al_4Cu_9 has been detected by XRD in this sample, TEM clearly shows its presence in the form of the γ-Al_4Cu_9 laths as well as spherical particles enveloped in the α-Cu matrix.

Adding tungsten in FSP resulted in enriching the samples with γ-Al_4Cu_9 so that corresponding XRD patterns clearly showed its reflections in addition to those of α-Cu and β'-Cu_3Al. Not much is known about nucleation and growth mechanisms of γ-Al_4Cu_9. It was, however, noted (Ref 29) that formation of γ-Al_4Cu_9 is often met with mechanical alloying on the Al-Cu powder mixtures or in friction stir welding (Ref 30). This IMC is of low thermal stability and may decompose into its components by heating to 180 °C (Ref 29) in contrast to β'-Cu_3Al whose peaks are still detectable even on annealing at 675 °C (Ref 31).

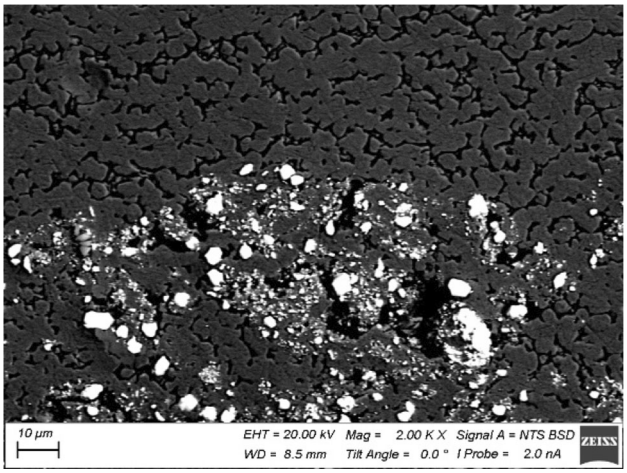

Fig. 16 SEM BSE microstructure images of CuAl9Mn2/10 vol.% W after 1-pass FSP

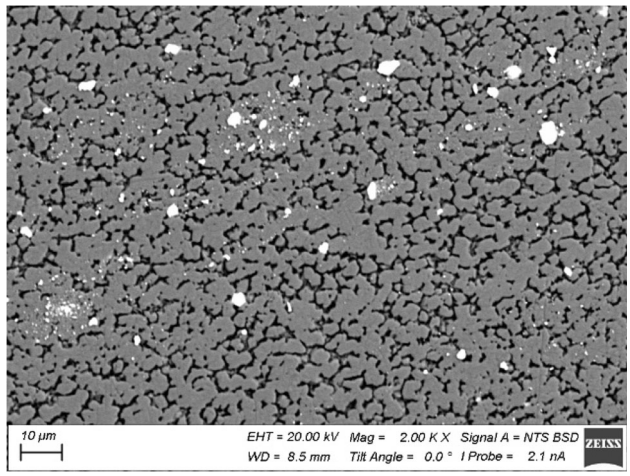

Fig. 18 SEM BSE microstructure images of CuAl9Mn2/10 vol.%W after 4-pass FSP

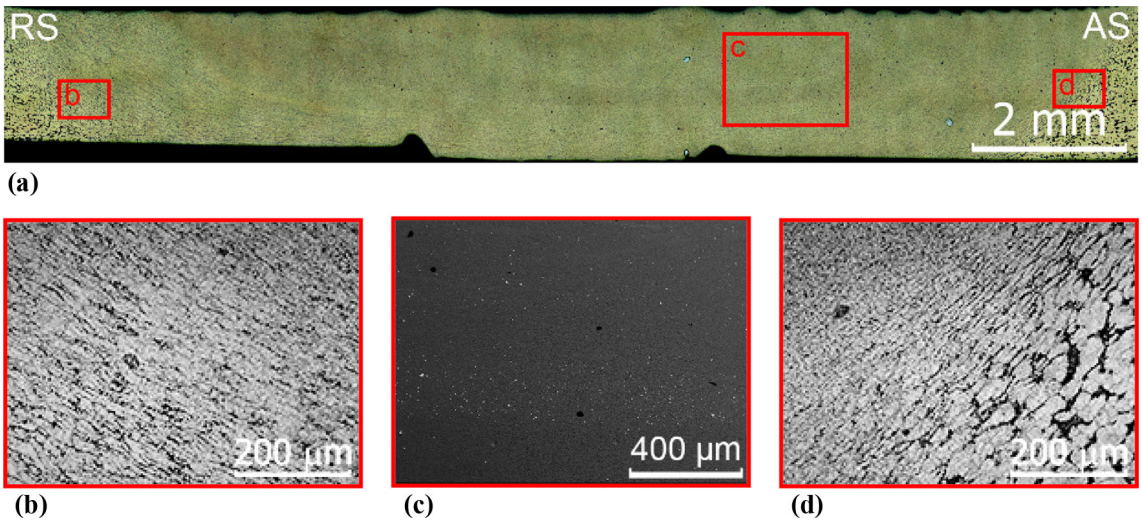

Fig. 17 Macrostructural optical image of structures formed in CuAl9Mn2/10 vol.% W by 4-pass FSP (a) and microstructures at the SZ/TMAZ boundary closer to RS (b), in SZ (c), and at SZ/TMAZ boundary closer to AS (d)

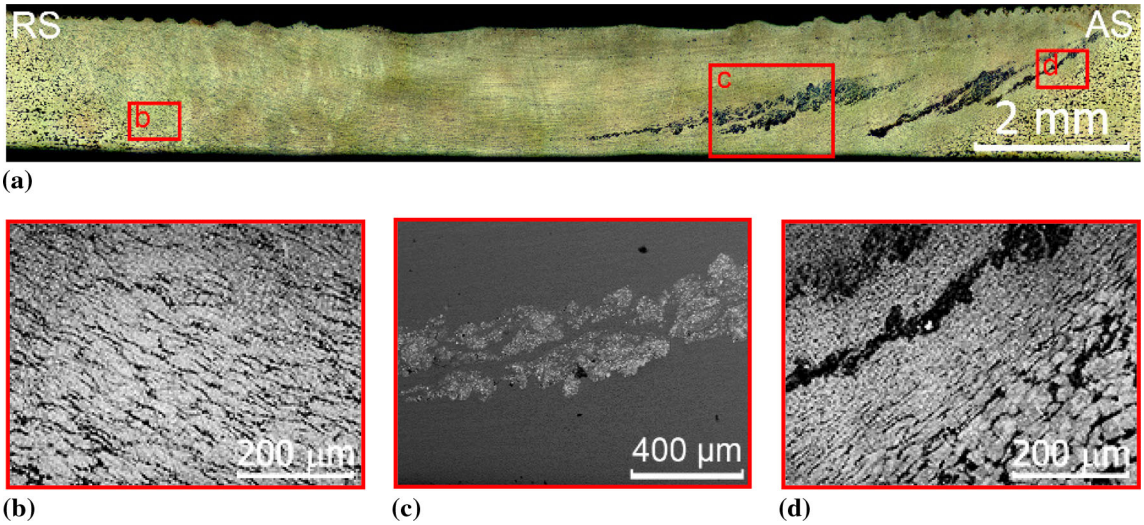

Fig. 19 Macrostructural optical image of structures formed in CuAl9Mn2/15 vol.% W by 1-pass FSP (a) and microstructures at the SZ/TMAZ boundary closer to RS (b), in SZ (c), and at SZ/TMAZ boundary closer to AS (d)

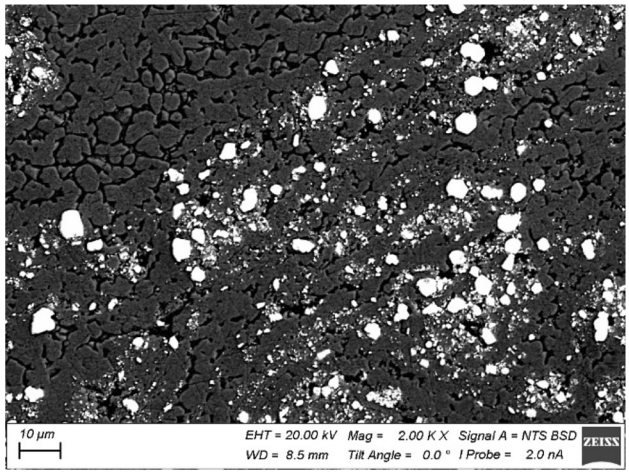

Fig. 20 SEM BSE microstructure images of CuAl9Mn2/15 vol.% W after 1-pass FSP

In this case, all the tungsten-containing samples revealed the presence of the γ-Al_4Cu_9 phase, while no tungsten-containing IMCs have been found in the them irrespective of the FSP pass number. The tungsten and copper are mutually immiscible metals, while reacting between tungsten and aluminum may require higher temperatures and higher concentrations of Al because here all the aluminum is bonded in the Al-Cu IMCs. In addition, only α-W was found both in the source powder and inside the composite. Therefore, formation of γ-Al_4Cu_9 according to the well-known equilibrium reaction $\beta \rightarrow \alpha + \gamma$ may be related to some physical characteristic of the composite that changed with the addition of tungsten. In our opinion, this could be the reduced heat conductivity that made some β-Cu_3Al grains to decompose into α-Cu and γ-Al_4Cu_9 ones instead of the $\beta \rightarrow \beta'$ transformation. This phase was also detected when adding titanium alloy to the manganese aluminum bronze using the electron beam additive manufacturing (Ref 32) when primary β-Cu_3Al grains decomposed into α-Cu, γ-Al_4Cu_9 and $TiCu_2Al$.

The presence of aluminum oxide traces was noted on the worn surfaces of FSPed bronze and composite samples (Fig. 32a, b), i.e., there occurred tribooxidation of the matrix alloy. Decomposition of γ-Al_4Cu_9 with oxidation is the most plausible during the tribooxidation. It was found that the amounts of tribooxidation products such as aluminum oxide and Cu_4Al decreased with the tungsten percentage. The reason behind such a finding maybe that tungsten oxides are formed on the real contact areas. These oxides possess low shear strength and can be easily smeared over the worn surface as a thin film, which may serve to inhibit the oxidation of matrix.

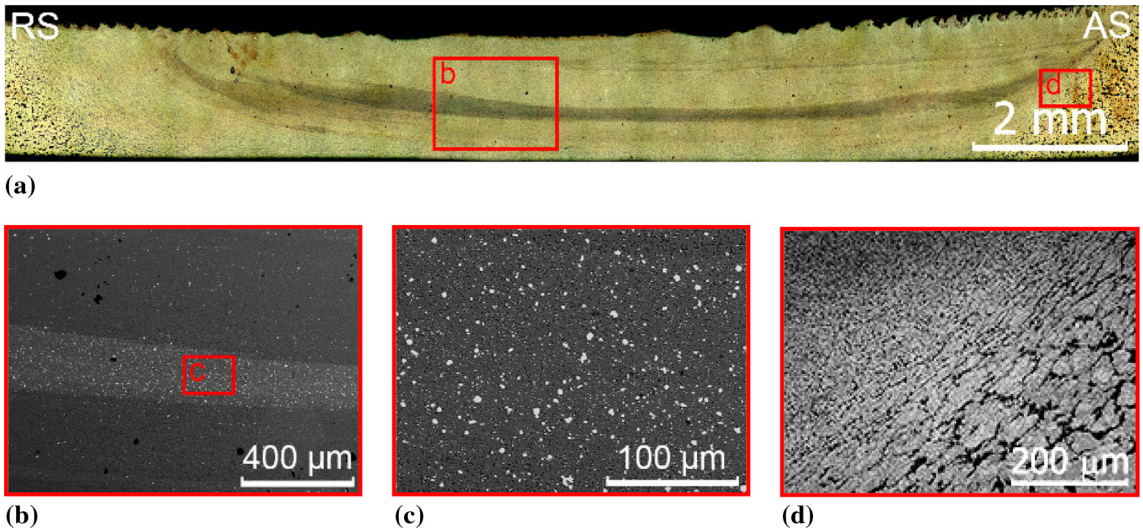

Fig. 21 Macrostructural optical image of structures formed in CuAl9Mn2/15 vol.% W by 4-pass FSP (a) and microstructures at the SZ/TMAZ boundary closer to RS (b), in SZ (c), and at SZ/TMAZ boundary closer to AS (d)

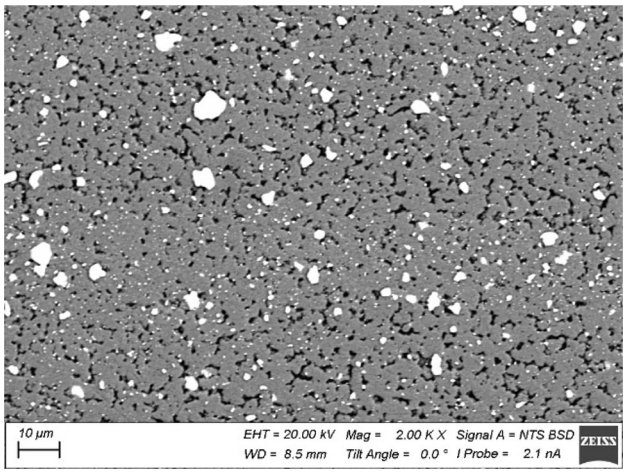

Fig. 22 SEM BSE microstructure images of CuAl9Mn2/15 vol.% W after 4-pass FSP.

4.2 Wear Behavior

The instability of tribological behavior is a drawback of aluminum bronzes that can be mended using heat treatment or reinforcing them with hard particles. Unlubricated sliding friction is often accompanied with generation of mechanically mixed layers that determine wear and friction characteristics under given load and sliding speed (Ref 33, 34). Adding reinforcement particles usually attain more stiffness to the bronzes with corresponding reduction in plastic deformation penetration, i.e., plastically deformed layer thickness. In addition, the reinforcement particles (or their fragments) are intermixed with the MML and thus make them stable against quasiviscous flow. One of the main mechanisms for generation of mechanically mixed layers (MML) is tribological intermixing of wear debris that result from both from sample and counterbody (Ref 33, 34). Tribological transfer and oxidation of the wear debris results in forming oxides of metals that belong to both parts of the tribologically mated couple (Ref 35-37).

The worn surfaces (Fig. 33, Table 5) as well as subsurface MML layers (Fig. 34, Table 6) of CuAl9Mn2-W samples subjected to rubbing against the steel counterbody are characterized by the absence of iron that is usually transferred from the steel counterbody. No iron oxides were detected also using the XRD on the worn surfaces of either FSP-ed bronze or FSP-ed bronze/W (Fig. 32).

Other researchers, however, reported on finding iron oxides on the worn surfaces of copper and bronze samples (Ref 35-38). The worn surfaces of laser fabricated by Wong et al. (Ref

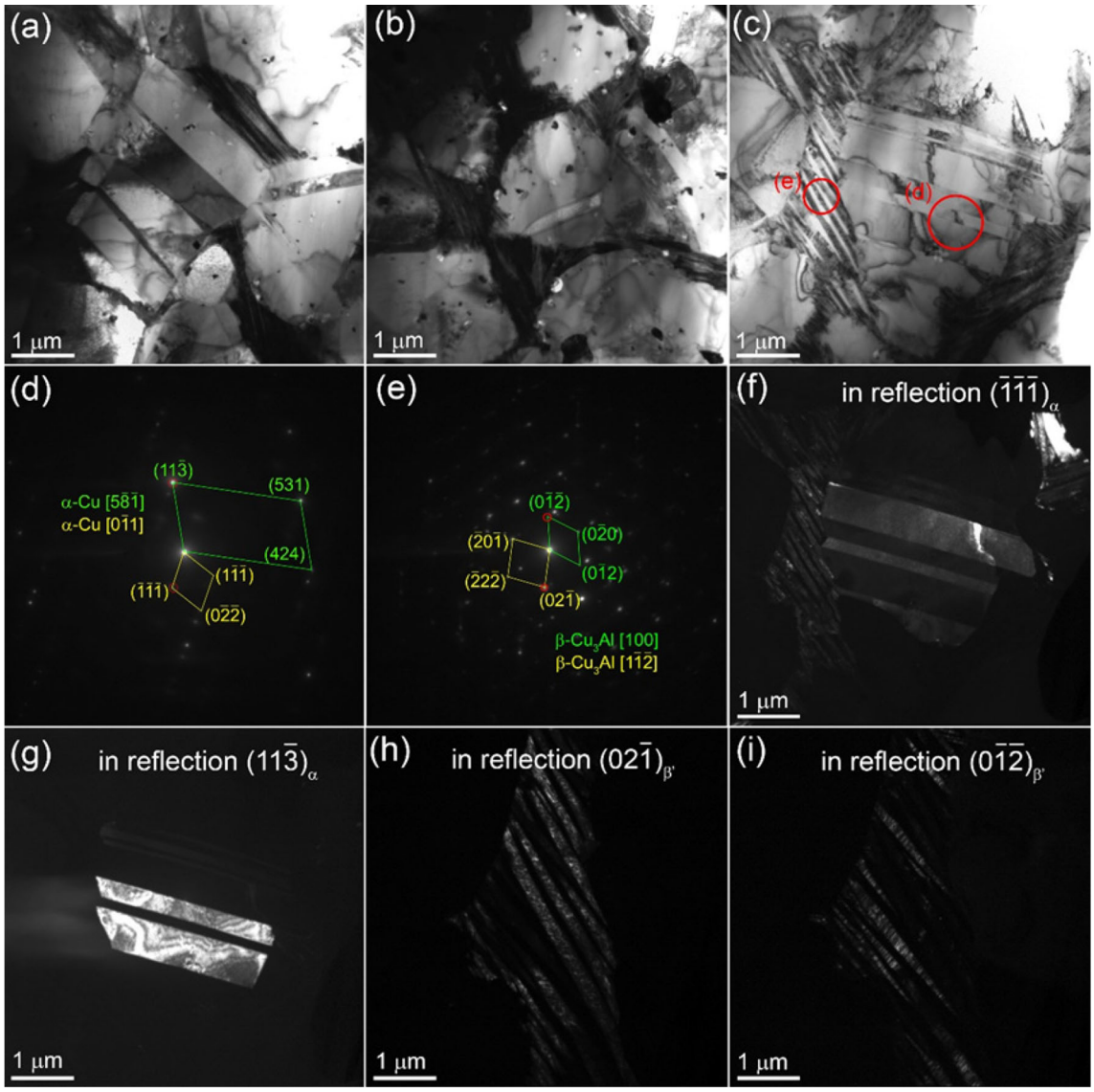

Fig. 23 Bright-field TEM images of microstructures in the CuAl9Mn2/15 vol.% W prepared using the 4-pass FSP (a–c), SAED patterns (d, e) obtained from zones inside the red circles (e, d) respectively, and dark-field TEM images (f–i), obtained using reflections $(\bar{1}\bar{1}\bar{1})_{\alpha}$, $(11\bar{3})\alpha$, $(02\bar{1})_{\beta'}$ and $(0\bar{1}2)_{\beta'}$

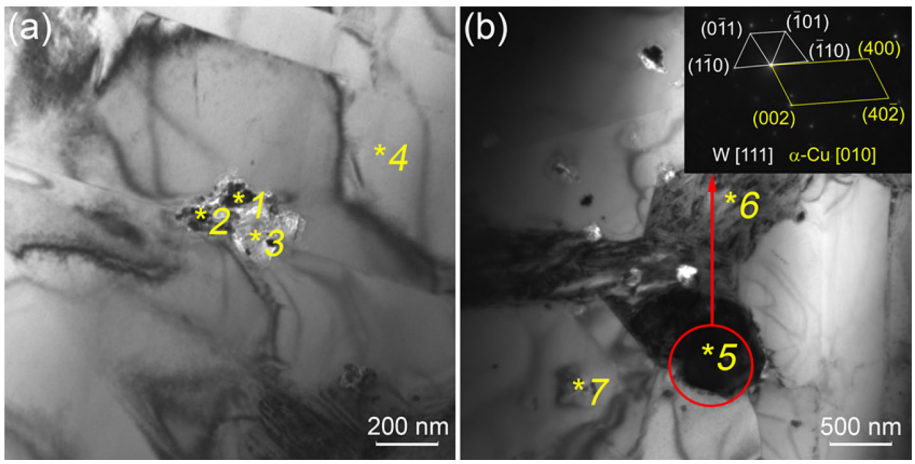

Fig. 24 Bright-field TEM images of microstructures in CuAl9Mn2/15 vol.% W prepared using the 4-pass FSP (a, b). 1-7 EDS probe zones

Table 4 EDS spectra obtained in zones indicated by figure 1-6 (Fig. 24)

Spectrum	Content, at.%					
	Al	Mn	Fe	Cu	W	Cr
1	21.7	2.5	2.2	60.9	12.7	…
2	21.2	9.8	5.0	58.6	5.4	…
3	29.2	2.2	2.1	66.6	…	…
4	10.8	1.9	0.5	86.7	…	…
5	…	0.3	2.2	39.2	56.7	1.6
6	17.9	2.3	1.6	77.7	0.2	0.3
7	27.1	1.71	0.44	66.31	4.14	0.3

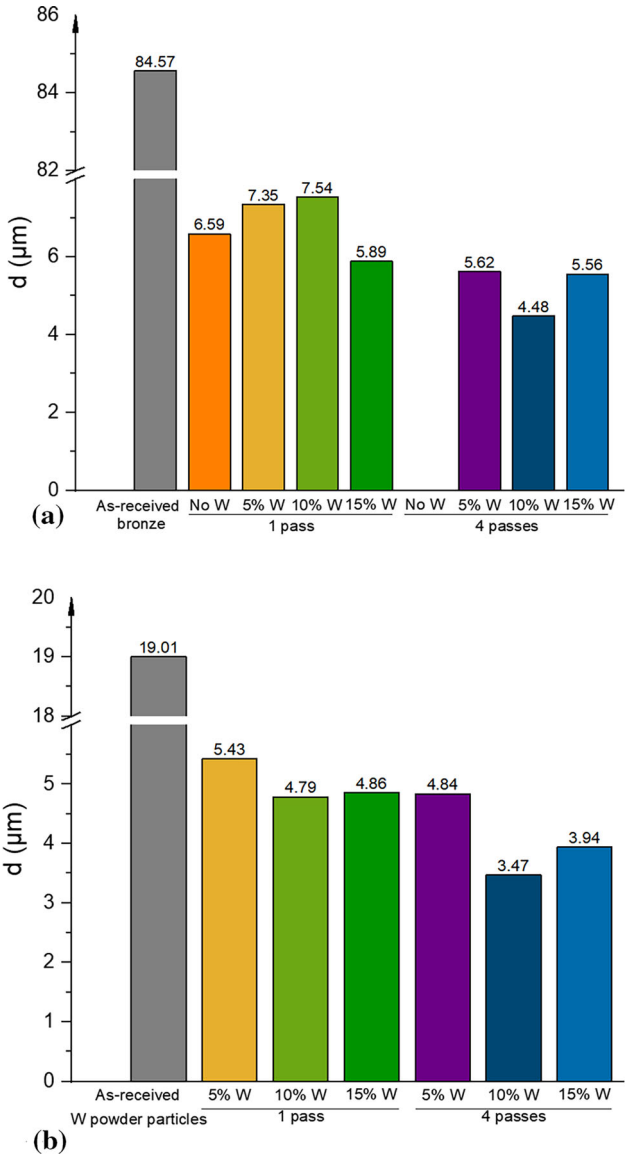

Fig. 25 Average grain size of the CuAl9Mn2 grains (a) and W particles (b) depending on the content of W and the number of passes FSP. Average grain size and grain size distribution in the 4-pass FSP-ed CuAl9Mn2/15 vol.% W

38) W-reinforced Cu layers contained iron after rubbing against a tool steel with hardness 600HV0.2 (54 HRC), while no transferred iron was detected on the W-25 wt.%Cu or W-31 wt.% composites rubbed against quenched and tempered to 64 HRC AISI 52100 counterbodies (Ref 15). Such a finding indicates on the counterbody's hardness as the main factor being responsible for iron transfer, and correspondingly, occurrence of the abrasive wear mechanism.

Along with that, the subsurface layered structures that form on the FSP-ed bronze/W samples in sliding may reduce the contact stress and thus reduce the effect of scratching the steel by hard particles (Fig. 34).

4.3 Subsurface Multilayer Structure

Generation of tribological layers in sliding of ductile materials was studied by many researchers, and it was shown that the on the first stage the main factors that contribute to generation of MML are subsurface plastic deformation, grain refining and frictional heating. On refining the grains to nanoscale level, these layers may form and flow as a quasiviscous medium and thus reveal a layered pattern as viewed in their cross section (Ref 39). The FSPed samples already contain the refined grain subgrained structures that are ready to participate in such a superplastic flow by means of intergrain slipping mechanism. This effect is observed in the multipass FSP when the second pass is carried out with the tool movement resistance considerably lower that of the first pass because of the refined grain structure (Ref 40). The tungsten agglomerates have already been crushed and densified in FSP but their further plastic deformation occurred below the worn surface so that they became elongated in the direction of the quasiviscous flow. In addition, the tribological layer contains high amount of oxygen that may oxidize the W particles and create tungsten oxide shells around them. If so then these particles would be less difficult to carry them along by the plastic flow trajectories.

Temperature on the contact areas is the most important factor of the subsurface plastic deformation. Therefore, it would be useful to estimate it using the well-known equation (1) (Ref 41):

$$\Delta T = \frac{\mu \mathrm{PV}}{4J\left(K_{\mathrm{sample}} + K_{\mathrm{disk}}\right)\alpha} \qquad \text{(Eq 1)}$$

where μ is the CoF, P and V are the normal load and sliding speed, respectively, and K_{sample} and K_{disk} are the thermal conductivities of the pin and disk, respectively. J is the Joule's constant (in this case, $J = 1$) and α is the contact radius of the real contact area to be determined from an equation as follows (2):

$$\alpha = \left(\frac{P}{\pi H_{\mathrm{sample}}}\right)^{1/2} \qquad \text{(Eq 2)}$$

where H_{sample} is the sample's hardness.

This flash temperature estimation was carried for the test parameters as follows: $P = 15$ N, hardness 1.2-2 GPa depending on composition (Fig. 27), $V = 0.26$ m/s and $\mu = 0.33$-0.36 depending on content (Fig. 31a, b). Thermal conductivity values of the Cu-W composites and AISI 52100 steel were in

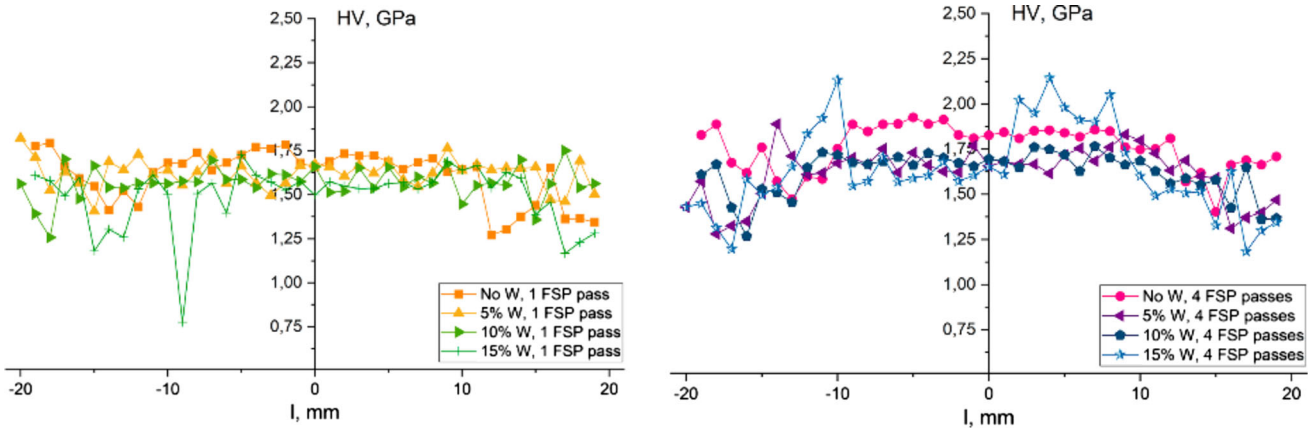

Fig. 26 Microhardness umbers distribution across the FSPed zone for samples with different content of W resulted from 1-pass (a) and 4-pass (b) FSP

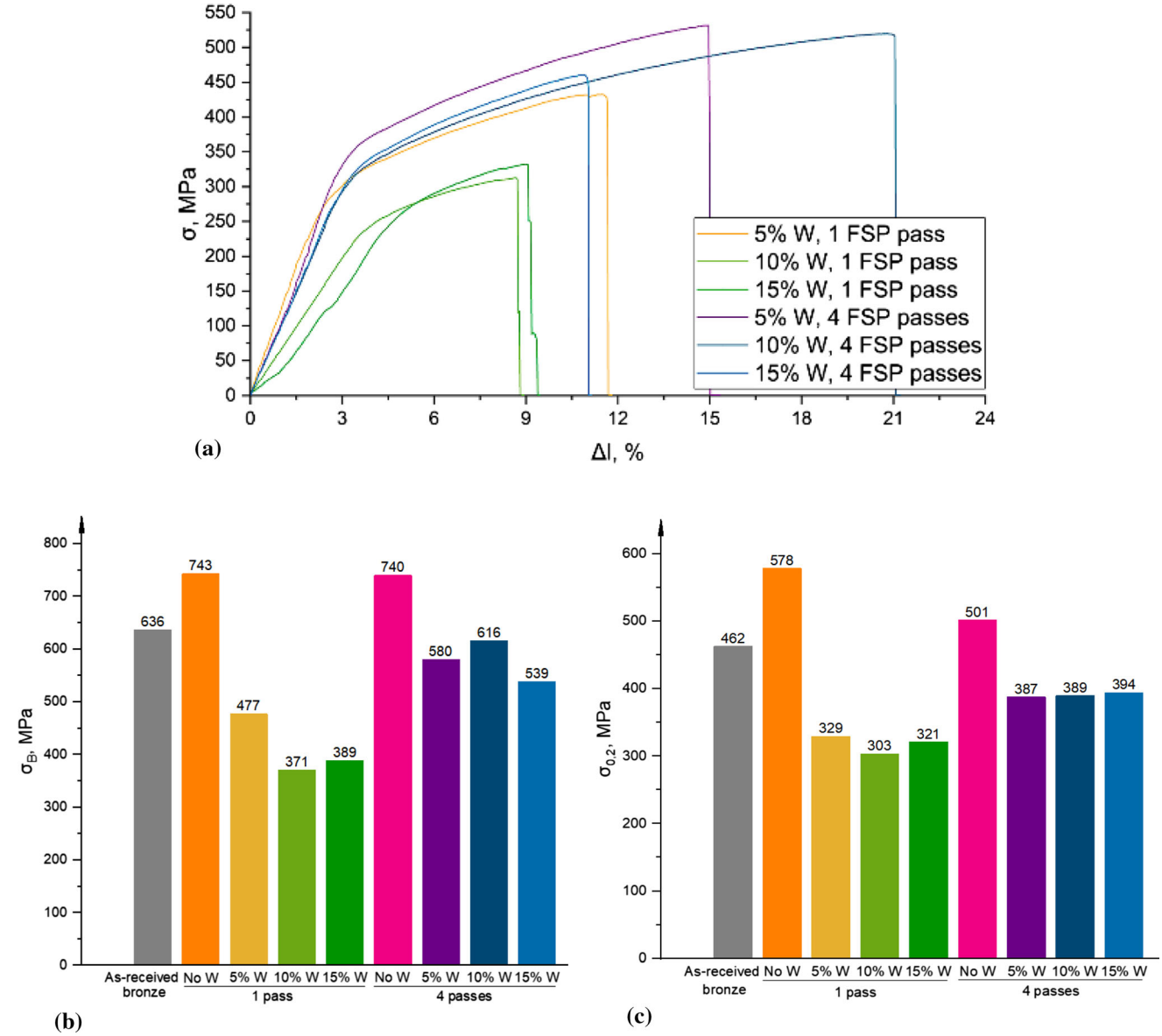

Fig. 27 Engineering tensile stress–strain curves (a), ultimate tensile strength (b) and yield stress (c) averaged values obtained on samples with different concentrations of W and different number of FSP passes

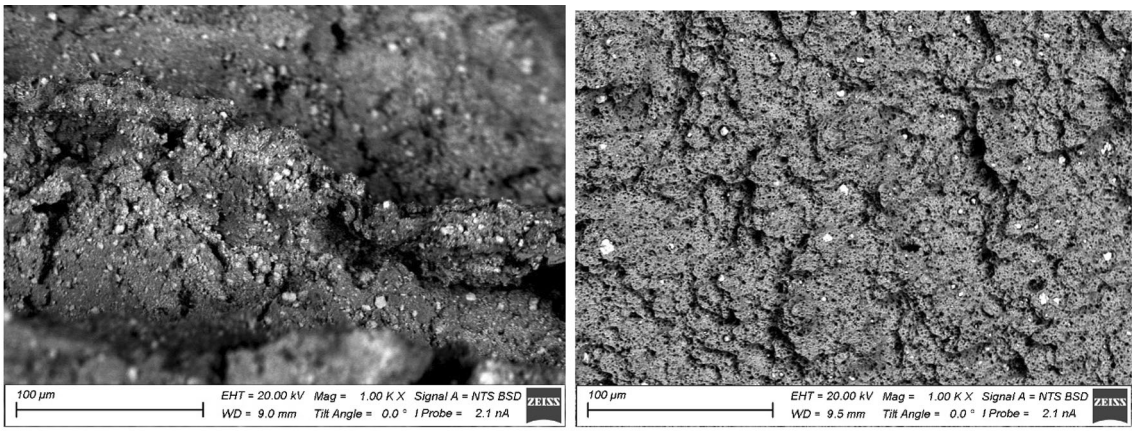

Fig. 28 SEM BSE images of the tensile test fracture surfaces of the FSP-ed bronze/5 vol.% W composites after 1 pass (a) and 4 passes (b)

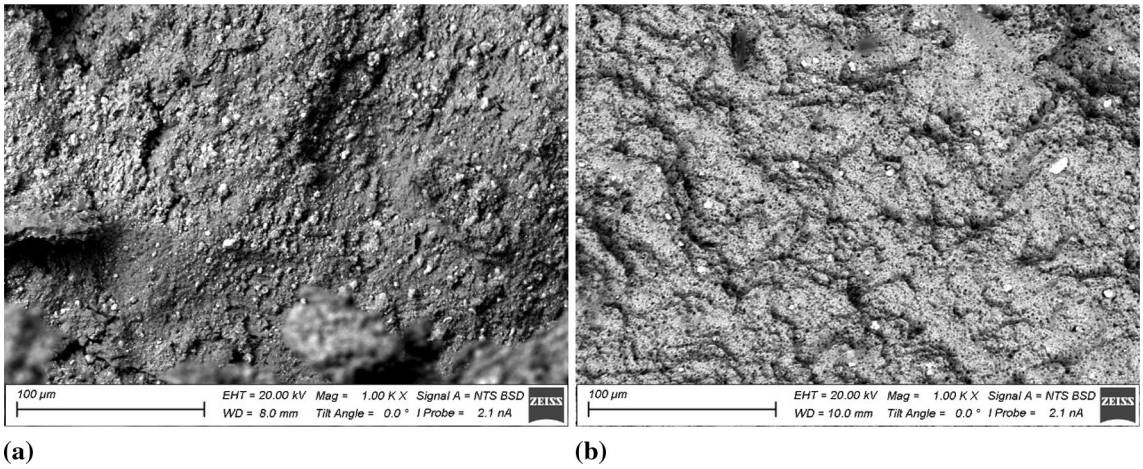

Fig. 29 SEM BSE images of the tensile test fracture surfaces of the FSP-ed bronze/10 vol.% W composites after 1 pass (a) and 4 passes (b)

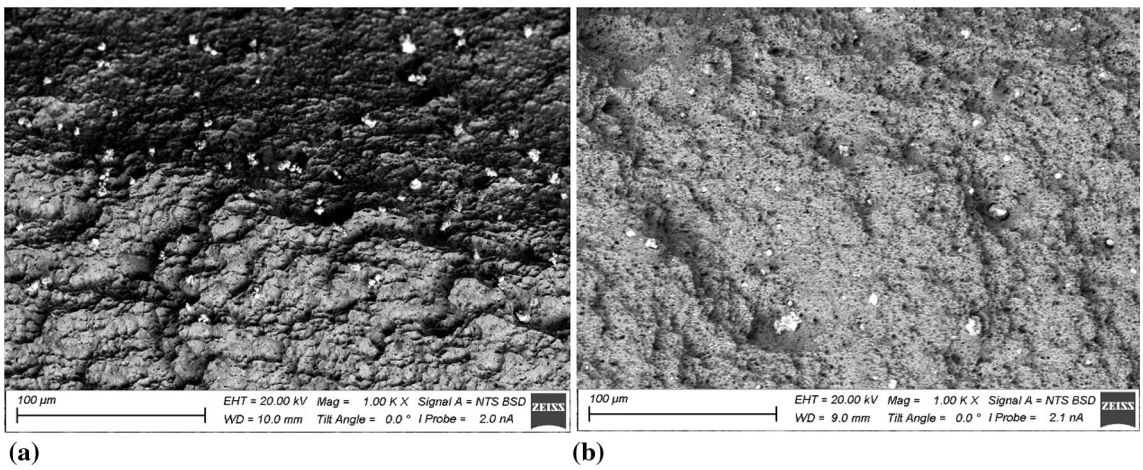

Fig. 30 SEM BSE images of the tensile test fracture surfaces of the FSP-ed bronze/15 vol.% W after 1 pass (a) and 4 passes (b)

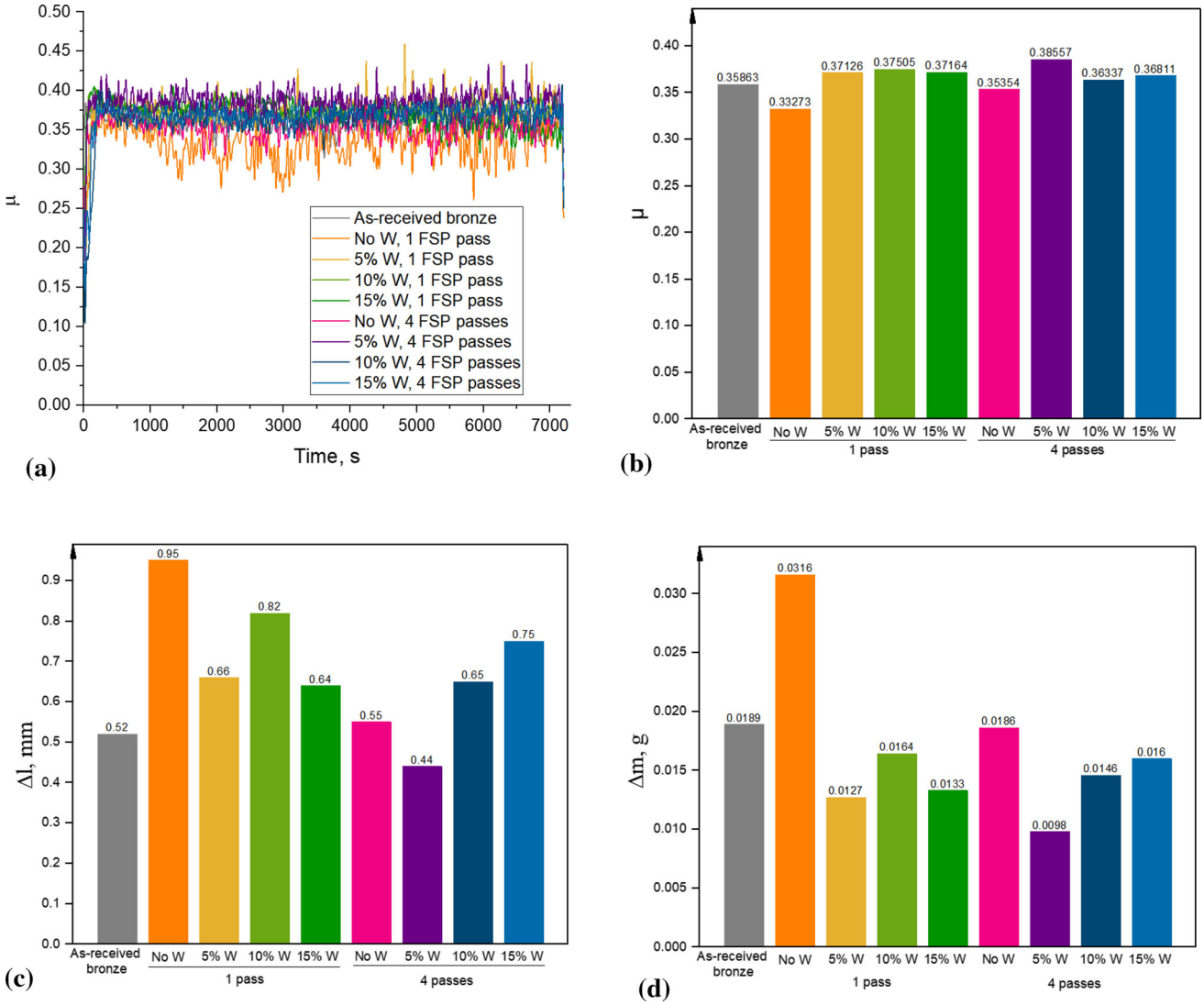

Fig. 31 CoF vs. time dependencies (a), CoF values as depended on the W percentage and FSP pass number (b), wear as estimated by the sample length reduction (c) and mass (d) losses in pin-on-disk sliding

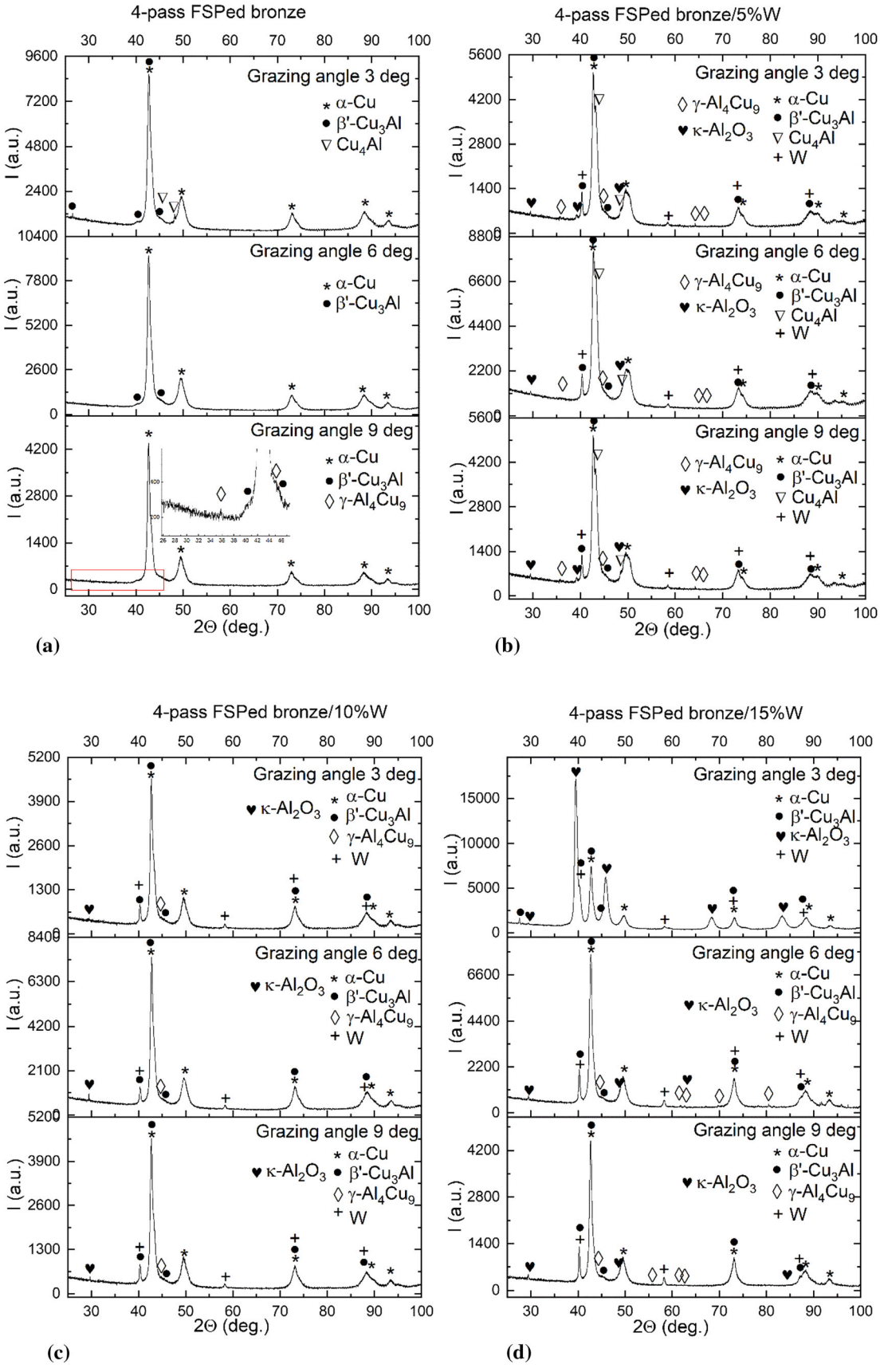

Fig. 32 Glancing x-ray diffractograms with the incidence angles of 9°, 6° and 3° from the worn surface of the FSP-ed bronze (a), FSP-ed bronze/5 vol.% W (b), FSP-ed bronze/10 vol.% W (c) and FSP-ed bronze/15 vol.% W (d). FSP-ed samples were obtained after 4 passes

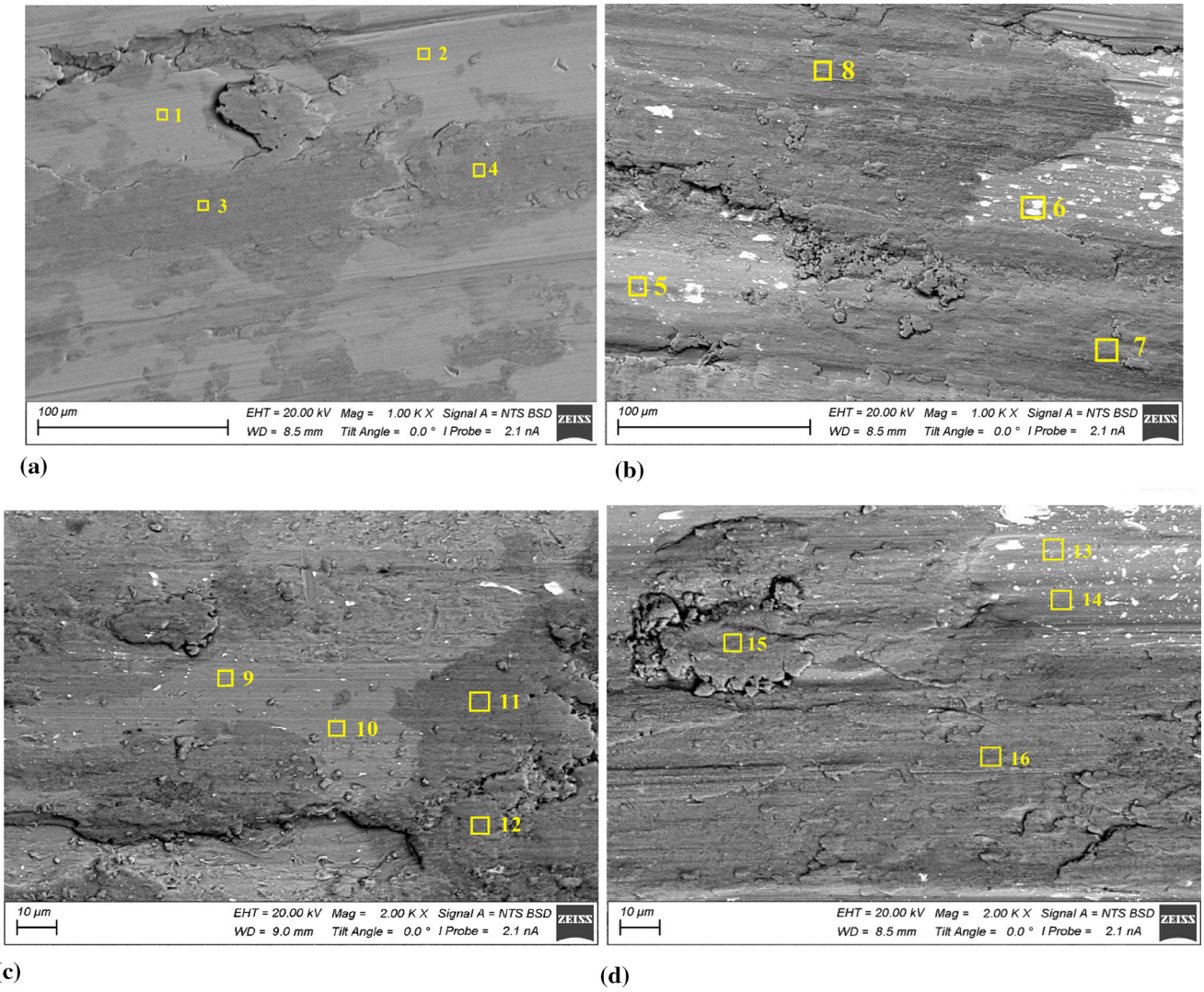

Fig. 33 SEM BSE worn surface images of the: (a) FSP-ed bronze after 4 passes, (b) FSP-ed bronze/5 vol.% W, (c) FSP-ed bronze/10 vol.% W, (b) FSP-ed bronze/15 vol.% W. FSP-ed samples were obtained after 4 passes. Numbers on (a–d) indicate probe zones for which EDS elemental concentrations were determined as indicated in Table 5

Table 5 EDS chemical composition of worn surface of the FSP-ed bronze (Fig. 33a), bronze/5 vol.% W (Fig. 33b), bronze/10 vol.% W (Fig. 33c), bronze/15 vol.% W (Fig. 33d)

	Element (at.%)					
Area	**O**	**Al**	**Mn**	**Cu**	**W**	**Fe**
Bronze						
1	…	16.19	1.79	82.02	…	…
2	…	19.65	2.51	77.84	…	…
3	25.50	11.02	1.30	62.17	…	…
4	21.51	12.29	1.49	64.72	…	…
Bronze/5 vol.% W						
5	…	20.07	1.72	75.14	3.07	…
6	…	…	…	41.05	58.95	…
7	34.26	15.37	…	47.95	0.66	…
8	46.93	16.79	1.78	33.54	0.95	…
Bronze/10 vol.% W						
9	…	18.97	1.81	79.22	…	…
10	…	17.15	2.04	80.82	…	…
11	30.26	11.35	1.58	56.16	0.66	…
12	26.81	11.78	1.64	59.78	…	…
Bronze/15 vol.% W						
13	…	18.25	2.10	75.84	3.81	…
14	…	19.82	1.75	78.43	19.82	…
15	13.69	13.52	1.75	70.23	0.81	…
16	18.33	9.53	1.51	69.94	0.69	…

the ranges 300-400 W m^{-1} K^{-1} and 44-50 W m^{-1} K^{-1} and were borrowed from the literature sources (Ref 42-44), respectively. The calculated flash temperatures were ≈27 ÷ 35 °C, that would be insufficient for intensification of the plastic flow. Nevertheless, the traces of such a flow were clearly observed and the reason behind it may be severe plastic deformation and residual plasticity of the composites.

Another problem with wear and friction on FSPed materials is that they loss their ductility due to their fine grain structure. Therefore, there is always a risk of overdeforming the material and thus obtaining wear by subsurface fracture. In connection with this, the multipass FSP is carried out using a limited number of passes. Similar effect may be obtained when adding too much reinforcement particles.

5. Conclusions

Friction stir processing was applied for preparing CuAl9Mn2/W composites by intermixing 0, 5, 10 and 15 vol.% W powder loaded into a system of holes drilled in a manganese aluminum bronze plate. The bronze was structurally composed of α-solid solution and β'-Cu_3Al phases. The 1-pass FSP was not enough to provide homogeneous distribution of the tungsten particles in the stir zone, which has been achieved only with the 4-pass FSP. The FSP resulted in forming intermetallic phase γ-Al_4Cu_9 in all samples. Adding more tungsten resulted in precipitation of more γ-Al_4Cu_9, which has been related to impairing the heat conductivity of the composite and suppression of the $\beta \rightarrow \beta'$ reaction in favor of $\beta \rightarrow \alpha + \gamma$ one. Tensile strength of the W-containing and FSPed composites have been impaired too as compared to that of as-received and FSPed bronze despite smaller grain structures. It was found that microhardness of the W-containing composites was at the level of FSPed as-received bronze irrespective of the FSP pass number.

Sliding wear tests showed the best wear resistance for samples FSPed with 5 vol.% W wherein effect of tribooxidation was accompanied by formation of κ-Al_2O_3 aluminum oxides by oxidation of metastable γ-Al_4Cu_9. All samples demonstrated the same value of the friction force in the range 0.30-0.40.

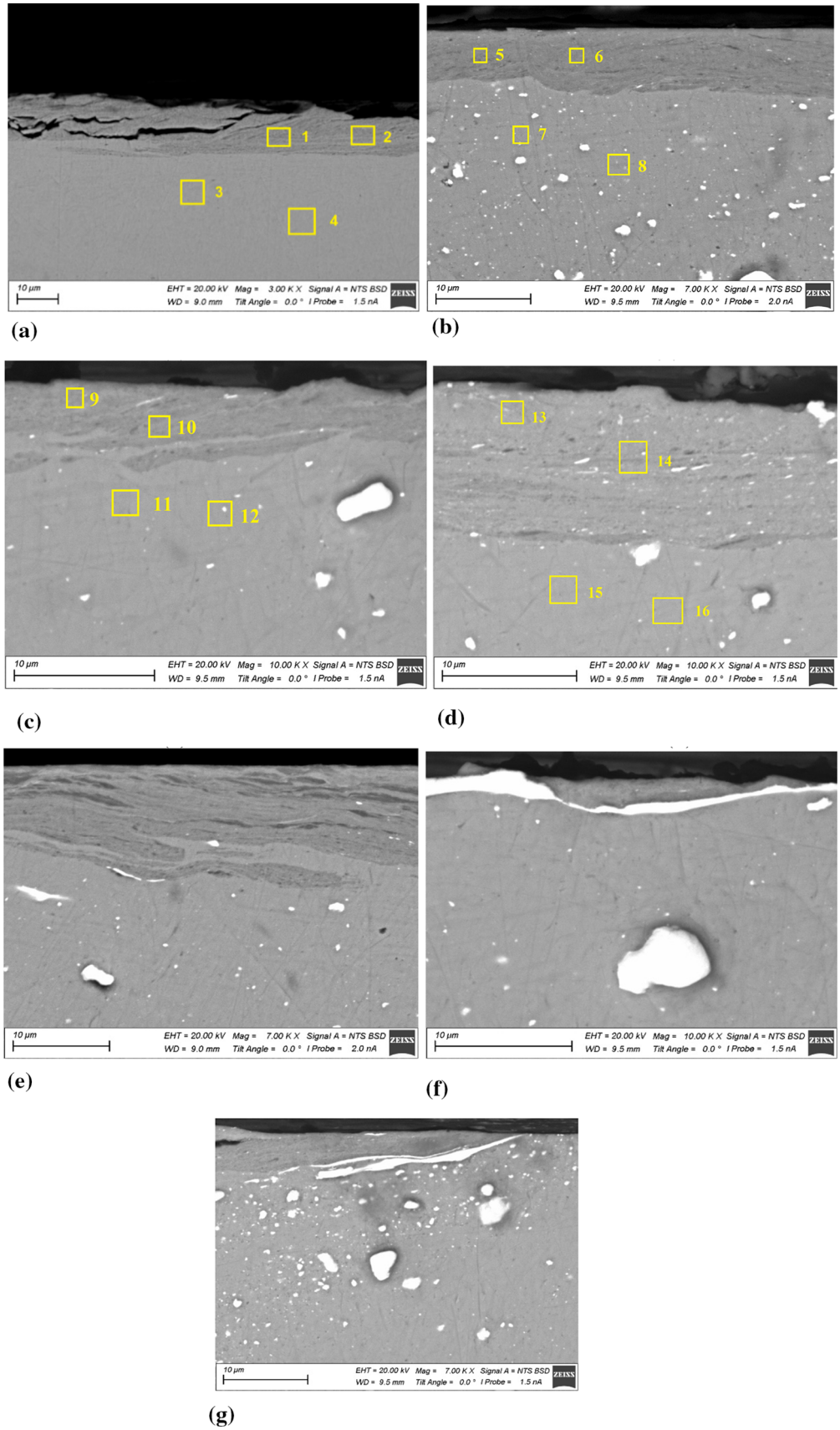

Fig. 34 SEM BSE images of microstructures formed by sliding below the worn surface of the: (a) FSP-ed bronze after 4 passes, (b, e) FSP-ed bronze/5 vol.% W, (c, f) FSP-ed bronze/10 vol.% W, (d, g) FSP-ed(bronze/15 vol.% W. These FSP-ed samples were obtained after 4 passes. Numbers on (a–d) indicate probe zones for which the EDS elemental concentrations were determined as indicated in Table 6

Table 6 EDS chemical composition of microstructures formed by sliding below the worn surface of the FSP-ed bronze (Fig. 34a), bronze/5 vol.% W (Fig. 34b), bronze/10 vol.% W (Fig. 34c), bronze/15 vol.% W (Fig. 34d)

	Element (at.%)					
Area	O	Al	Mn	Cu	W	Fe
Bronze						
1	23.33	14.79	1.64	60.23	…	…
2	13.08	16.46	1.52	68.96	…	…
3	…	15.42	1.85	82.73	…	…
4	…	16.49	1.75	81.76	…	…
Bronze/5 vol.% W						
5	31.21	13.14	1.33	54.32	…	…
6	31.58	13.53	1.05	53.05	0.79	…
7	…	18.46	2.12	74.97	4.46	…
8	…	17.42	1.86	79.61	1.11	…
Bronze/10 vol.% W						
9	7.55	6.78	1.48	78.90	5.29	…
10	7.50	5.73	1.77	82.24	2.75	…
11	…	7.08	1.98	90.95	…	…
12	…	7.64	2.41	89.94	…	…
Bronze/15 vol.% W						
13	3.74	8.85	1.51	81.72	4.17	…
14	4.27	7.46	1.73	82.66	3.88	…
15	…	7.72	1.84	90.44	…	…
16	…	9.53	1.51	69.94	…	…

Acknowledgments

The investigations have been carried out using the equipment of Share Use Centre "Nanotech" of the ISPMS SB RAS.

Author contribution

A.Z., N.S., A.C. and S.T. were involved in the conceptualization; A.Z., N.S., and A.C. contributed to the methodology; A.V. and N.S. contributed to the software; A.C., A.Z., and N.S. assisted in the validation; A.Z., N.S., A.C. and S.T. performed the formal analysis; A.Z., E.K., N. S., D.G., A.V., V.U., N.S. and A.C. contributed to the investigation; A. Chum. and E.K. contributed to the resources; A.C., A.Z., N.S., and A.C. curated the data; A.C., A.Z., N.S., and S.T. contributed to writing—original draft preparation; A.Z., N.S., and S.T. assisted in writing—review and editing; A.Z., E.K., N. S., D.G., A.V., V.U., N. S. and A.C. contributed to the visualization; A.Z. and S.T. contributed to the supervision; A.Z. and A.C. were involved in the project administration; A.C. acquired the funding. All authors have read and agreed to the published version of the manuscript.

Funding

This research was funded by Government research assignment for ISPMS SB RAS, project FWRW-2024-0001.

Data availability

The authors confirm that the data supporting the findings of this study are available within the article. All data necessary for the replication of results are provided within the paper.

Code availability

Not applicable.

Conflict of interest

The authors declare no conflict of interest.

Ethical approval

Not applicable.

Consent to participation

Not applicable.

Consent for publication

Not applicable.

References

1. S. Wan, X. Cui, Q. Jin, J. Ma, X. Wen, W. Su, X. Zhang, G. Jin and H. Tian, Microstructure and Properties of Cold Sprayed Aluminum Bronze Coating on MBLS10A-200 Magnesium-Lithium Alloy, *Mater. Chem. Phys.*, 2020, **281**, p 125832. https://doi.org/10.1016/j.matchemphys.2022.125832
2. T. Lu, C. Chen, P. Li, Ch. Zhang, W. Han, Z. Ya, Ch. Suryanarayana and Zh. Guo, Enhanced Mechanical and Electrical Properties of In Situ Synthesized Nano-Tungsten Dispersion-Strengthened Copper Alloy, *Mater. Sci. Eng. A*, 2021, **799**, p 140161. https://doi.org/10.1016/j.msea.2020.140161
3. M.V. Lungu, D. Pătroi, V. Marinescu, S. Mitrea, I. Ion, M. Marin and P. Godeanu, Tungsten–Copper Composites for Arcing Contact Applications in High Voltage Circuit Breakers, *Mater. Sci. Res. India*, 2020, **17**(3), p 214–229. https://doi.org/10.13005/msri/170304
4. L.L. Dong, M. Ahangarkani, W.G. Chen and Y.S. Zhang, Recent Progress in Development of Tungsten-Copper Composites: Fabrication, Modification and Applications, *Intl. J. Refract. Hard Met.*, 2018, **75**, p 30. https://doi.org/10.1016/j.ijrmhm.2018.03.014
5. Q. Zhang, Sh. Liang and L. Zhuo, Fabrication and Properties of the W-30wt.%Cu Gradient Composite with W@WC Core-Shell Structure, *J. Alloys Compd.*, 2017, **708**, p 796–803. https://doi.org/10.1016/j.jallcom.2017.03.064
6. Y. Huang, X. Zhou, N. Hua, W. Que and W. Chen, High Temperature Friction and Wear Behavior of Tungsten–Copper Alloys, *Int. J. Refract. Met. Hard Mater.*, 2018, **77**, p 105–112. https://doi.org/10.1016/j.ijrmhm.2018.08.001
7. F. Ren, W. Zhu, K. Chu and C. Zhao, Tribological and Corrosion Behaviors of Bulk Cu-W Nanocomposites Fabricated by Mechanical Alloying and Warm Pressing, *J. Alloy. Compd.*, 2016, **676**, p 164–172. https://doi.org/10.1016/j.jallcom.2016.03.141
8. W. Chen, P. Feng, L. Dong, M. Ahangarkani, Sh. Ren and Y. Fud, The Process of Surface Carburization and High Temperature Wear Behavior of Infiltrated W-Cu Composites, *Surf. Coat. Technol.*, 2018, **353**, p 300–308. https://doi.org/10.1016/j.surfcoat.2018.08.088
9. M. Hashempour, H. Razavizadeh and H. Rezaie, Investigation on Wear Mechanism of Thermochemically Fabricated W-Cu Composites, *Wear*, 2010, **269**(5–6), p 405–415. https://doi.org/10.1016/j.wear.2010.04.026
10. A. Pervikov, A. Filippov, Yu. Mironov, M. Kalashnikov, M. Krinitcyn, D. Eskin, M. Lerner and S. Tarasov, Microstructure and Properties of a

Nanostructured W-31 wt.% Cu Composite Produced by Magnetic Pulse Compaction of Bimetallic Nanoparticles, *Intl. J. Refract. Hard Met.*, 2022, **103**, p 105735. https://doi.org/10.1016/j.ijrmhm.2021.105735

11. H. Yo, X. Zhou, N. Hua, W. Que and W. Chen, High Temperature Friction and WEAR Behavior of Tungsten–Copper Alloys, *Intl. J. Refract. Hard Met.*, 2018, **77**, p 105–112. https://doi.org/10.1016/j.ijrmhm.2018.08.001
12. C.L. Wang, Y. Gao and G.Y. Zhang, Microstructure and wear Resistance of Cu-W Alloy Contact Material Prepared by Laser Shock Processing, *T. Mater. Heat Treat.*, 2014, **35**, p 153–155. https://doi.org/10.1016/j.jallcom.2016.03.141
13. F.M. Wang, J.P. Xie, Y. Li and A.Q. Wang, Dry-Sliding Tribological Characteristics of W80C20 Composite under of Magnetic Field, *Chin. Sur. Eng.*, 2014, **27**, p 76–79
14. Yu. Li, Ch. Hou, L. Cao, Ch. Liu, Sh. Liang, F. Tang, X. Song and Z. Nie, Excellent Wear Resistance of Multicomponent Nanocrystalline W-Cu Based Composite, *J. Alloys Compd.*, 2021, **861**, p 158627. https://doi.org/10.1016/j.jallcom.2021.158627
15. M. Jahangiri, M. Hashempour, H. Razavizadeh and H.R. Rezaie, A New Method to Investigate the Sliding Wear Behaviour of Materials based on Energy Dissipation: W–25 wt.%Cu Composite, *Wear*, 2012, **274–275**, p 175–182. https://doi.org/10.1016/j.wear.2011.08.023
16. X. Wang, X. Zhang, L. Zhao, Ch. Zhao, H. Zhang, Du. Ye, W. Zhang, G. Ya and P. Cao, Tungsten/copper Composite Sheets Prepared by a Novel Encapsulation Rolling TECHNIQUE, *J. Alloys Compd.*, 2021, **884**, p 161051. https://doi.org/10.1016/j.jallcom.2021.161051
17. Ch. Hou, X. Song, F. Tang, L. Yurong, L. Cao, J. Wang and Z. Nie, W-Cu Composites with Submicron- and Nanostructures: Progress and Challenges, *NPG Asia Mater.*, 2019, **11**(1), p 74. https://doi.org/10.1038/s41427-019-0179-x
18. K.S. Mohammed, A. Rahmat and A. Aziz, Self-Compacting High Density Tungsten–Bronze Composites, *J. Mater. Process. Technol.*, 2013, **213**, p 1088–1094. https://doi.org/10.1016/j.jmatprotec.2013.02.006
19. M. Pezeshkian and I. Ebrahimzadeh, Investigating the Role of Metal Reinforcement Particles in Producing Cu/Ni/W Metal Matrix Composites via Friction Stir Processing: Microstructure, Microhardness, and Wear at High Temperature, *Met. Mater. Int.*, 2023 https://doi.org/10.1007/s12540-023-01488-6
20. V. Sharma, U. Prakash and B.V. Manoj Kumar, Surface Composites by Friction Stir Processing: A Review, *J. Mater. Process. Technol.*, 2015, **224**, p 117–134. https://doi.org/10.1016/j.jmatprotec.2015.04.019
21. A. Zykova, A. Chumaevskii, A. Gusarova, D. Gurianov, T. Kalashnikova, N. Savchenko, E. Kolubaev and S. Tarasov, Evolution of Microstructure in friction Stir Processed Dissimilar CuZn37/AA5056 Stir Zone, *Materials*, 2021, **14**(18), p 5208. https://doi.org/10.3390/ma14185208
22. A.P. Zykova, S.Y. Tarasov, A.V. Chumaevskiy and E.A. Kolubaev, A Review of Friction Stir Processing of Structural Metallic Materials: Process, Properties, and Methods, *Met.*, 2020, **10**(6), p 772. https://doi.org/10.3390/met10060772
23. A. Zykova, A. Vorontsov, A. Chumaevskii, D. Gurianov, A. Gusarova, E. Kolubaev and S. Tarasov, Structural Evolution of Contact Parts of the Friction Stir Processing Heat-Resistant Nickel Alloy Tool Used for Multi-Pass Processing of Ti6Al4V/(Cu+Al) System, *Wear*, 2022, **488–489**, p 204138. https://doi.org/10.1016/j.wear.2021.204138
24. Y. Ahuja, R. Ibrahim, A. Paradowska and D. Riley, Friction Stir Forming to Fabricate Copper-Tungsten Composite, *J. Mater. Process. Technol.*, 2015, **217**, p 222–231. https://doi.org/10.1016/j.jmatprotec.2014.11.024
25. M. Sabbaghian, M. Shamanian, H.R. Akramifard and M. Esmailzadeh, Effect of Friction Stir Processing on the Microstructure and Mechanical Properties of Cu-TiC Composite, *Ceram. In.*, 2014, **40**(8), p 12969–12976. https://doi.org/10.1016/j.ceramint.2014.04.158
26. M. Barmouz and M.K.B. Givi, Fabrication of In Situ Cu/SiC Composites using Multi-Pass Friction Stir Processing: Evaluation of Microstructural, Porosity, Mechanical and Electrical Behavior, *Compos. Part A Appl. Sci. Manuf.*, 2011, **42**, p 1445–1453. https://doi.org/10.1016/j.compositesa.2011.06.010
27. V. Rubtsov, A. Chumaevskii, A. Gusarova, E. Knyazhev, D. Gurianov, A. Zykova, T. Kalashnikova, A. Cheremnov, N. Savchenko, A. Vorontsov, V. Utyaganova, E. Kolubaev and S. Tarasov, Macro- and Microstructure of In Situ Composites Prepared by Friction Stir Processing of AA5056 Admixed with Copper Powders, *Mater.*, 2023, **16**, p 1070. https://doi.org/10.3390/ma16031070
28. Y.P. Mironov, L.L. Meisner and A.I. Lotkov, The Structure of Titanium Nickelide Surface Layers Formed by Pulsed Electron-Beam Melting, *Tech. Phys.*, 2008, **53**, p 934–942. https://doi.org/10.1134/s1063784208070189/metrics
29. R. Besson, M.-N. Avettand-Fenoel, L. Thuinet, J. Kwon, A. Addad, P. Roussel and A. Legris, Mechanisms of Formation of Al_4Cu_9 during Mechanical Alloying: An Experimental Study, *Acta Mater. Mater.*, 2015, **87**, p 216–224. https://doi.org/10.1016/j.actamat.2014.12.050
30. Q. Zhang, W. Gong and W. Liu, Microstructure and Mechanical Properties of Dissimilar Al−Cu Joints by Friction Stir Welding, *Trans. Nonferrous Met. Soc. China*, 2015, **25**, p 1779–1786. https://doi.org/10.1016/S1003-6326(15)63783-9
31. A. Zykova, A. Panfilov, A. Chumaevskii, A. Vorontsov, D. Gurianov, N. Savchenko, E. Kolubaev and S. Tarasov, Decomposition of β′-Martensite in Annealing the Additively Manufactured Aluminum Bronze, *Mater. Lett.*, 2023, **338**, p 134064. https://doi.org/10.1016/j.matlet.2023.134064
32. A. Zykova, A. Nikolaeva, A. Panfilov, A. Vorontsov, A. Nikonenko, A. Dobrovolsky, A. Chumaevskii, D. Gurianov, A. Filippov, N. Semenchuk, N. Savchenko, E. Kolubaev and S. Tarasov, Microstructures and Phases in Electron Beam Additively Manufactured Ti-Al-Mo-Zr-V/CuAl9Mn2, *Alloy Mater.*, 2023, **16**, p 4279. https://doi.org/10.3390/ma16124279
33. J. Schell, P. Heilmann and D.A. Rigney, Friction and Wear of Cu–Ni Alloys, *Wear*, 1982, **75**, p 205–220. https://doi.org/10.1016/0043-1648(82)90149-1
34. B. Venkataraman and G. Sundararajan, The Sliding Wear Behaviour of Al–SiC Particulate Composites. II. The Characterization of Subsurface Deformation and Correlation with Wear Behavior, *Acta Mater. Mater.*, 1996, **44**, p 461–473. https://doi.org/10.1016/1359-6454(95)00218-9
35. W. Czupryk, Frictional Transfer of Iron in Oxidative Wear Conditions during Lubricated Sliding, *Wear*, 2000, **237**, p 288–294. https://doi.org/10.1016/S0043-1648(99)00360-9
36 J.B. Singh, J.G. Wen and P. Bellon, Nanoscale Characterization of the Transfer Layer Formed During Dry Sliding of Cu–15wt.% Ni–8wt.% Sn Bronze Alloy, *Acta Mater. Mater.*, 2008, **56**(13), p 3053–3064. https://doi.org/10.1016/0043-1648(82)90149-1
37. W. Cai and P. Bellon, Subsurface Microstructure Evolution and Deformation Mechanism of Ag–Cu Eutectic Alloy After Dry Sliding Wear, *Wear*, 2013, **303**(1), p 602–610. https://doi.org/10.1016/j.wear.2013.04.006
38. P.K. Wong, C.T. Kwok, H.C. Ma and D. Guo, Laser Fabrication of W-Reinforced Cu Layers II. Electrical Wear Behavior in Air and Synthetic Acid Rain, *Mater. Chem. Phys.*, 2016, **177**, p 118–130. https://doi.org/10.1016/j.matchemphys.2016.04.00
39 S. Tarasov, V. Rubtsov and A. Kolubaev, Subsurface Shear Instability and Nanostructuring of Metals in Sliding, *Wear*, 2010, **268**(1–2), p 59–66. https://doi.org/10.1016/j.wear.2009.06.027
40. K.N. Kalashnikov, SYu. Tarasov, A.V. Chumaevskii, S.V. Fortuna, A.A. Eliseev and A.N. Ivanov, Towards Aging in a Multipass Friction Stir–Processed AA2024, *Int. J. Adv. Manuf. Technol.*, 2019, **103**, p 2121–2132. https://doi.org/10.1007/s00170-019-03631-3
41. Y. Li, H. Fu, T. Ma, K. Wang, X. Yang and J. Lin, Microstructure and Wear Resistance of AlCoCrFeNi-WC/TiC Composite Coating by Laser Cladding, *Mater Charact*, 2022, **194**, p 112479. https://doi.org/10.1016/j.matchar.2022.112479
42. Y.D. Kim, N.L. Oh, S.-T. Oh and I.-H. Moon, Thermal Conductivity of W-Cu Composites at Various Temperatures, *Mater. Lett.*, 2001, **51**, p 420–424. https://doi.org/10.1016/S0167-577X(01)00330-5
43. M. Jamil, N. He, W. Zhao, A.M. Khan, H. Xiang, M.K. Gupta and A. Iqbal, A Novel Low-Pressure Hybrid Dry Ice Blasting System For Improving the Tribological and Machining Characteristics of AISI-52100 Tool STEEL, *J. Manuf. Process.*, 2022, **80**, p 152–160. https://doi.org/10.1016/J.JMAPRO.2022.05.056
44. B. Denkena, A. Krödel and A. Heckemeyer, Numerical and Experimental Analysis of Thermal and Mechanical Tool Load When Turning AISI 52100 with Ground Cutting Edge Microgeometries, *CIRP J.*

Manuf. Sci. Technol., 2021, **35**, p 494–501. https://doi.org/10.1016/J.CIRPJ.2021.08.006